Leiden University

Leiden Observatory

Prototyping LOUPE

The design and construction of the first iteration of the Lunar Observatory for Unresolved Polarimetry of Earth

Author:
H.J. Hoeijmakers B.Sc.

Supervisor:
Prof. Dr. C.U. Keller

August 22, 2013

Abstract

Based on the proposal presented by Karalidi et al. (2012), we have designed and built a prototype for the Lunar Observatory for Unresolved Polarimetry of Earth. LOUPE is to perform disk-integrated Earth-observations from the surface of the Moon, with the goal of extracting the polarization spectrum of Earth for all of its phase angles and diurnal phases. The observations will span visible wavelengths, roughly between $400 - 800$ nm (including the O_2A absorption feature at 760 nm) and maintain spatial resolution across the Earth's disk, to allow for a disentanglement of the contribution of different surface features to the global polarization signal. These observations will be crucial for independent verification of radiative transfer models of exoplanets, in which polarimetry plays an important role. A working version of LOUPE was constructed to demonstrate that the scientific requirements for these observations can be met using only solid state optics. The dimensions of the prototype are roughly $6 \times 6 \times 42\text{cm}^3$ and we are confident that the actual flight model can be miniaturized significantly, making LOUPE an appealingly small and robust instrument to be added to the arsenal of any future lunar landing vehicle. Test observations on targets in the laboratory show that the requirements on the spectral, imaging and polarization properties are very likely to be met and at the time of writing, efforts are being made to prepare the instrument for lunar observations, to demonstrate LOUPE's merit outside the laboratory environment.

Contents

Acknowledgements

I would like to express my gratitude to everyone who has contributed to the development of this instrument, an endeavour which continues to be highly successful, in the opinion of the author. Special words of thanks go to Frans Snik for his uninterrupted availability to render support and provide feedback, as well as to Michiel Rodenhuis without whom's objective lenses the expansion of LOUPE to include imaging capability would have been prohibitively tedious. Finally, I would like to thank Sara Khalafinejad for her assistance while aligning and photographing the last iteration of the prototype setup, during what should have been only a short lab tour.

Chapter 1

Introduction

1.1 History of the search for Earth-like exoplanets

For centuries, scholars have theorized about life on other worlds. With the discovery of exoplanets in the mid 1990s, the possibility of finding extraterrestrial life departed from the realm of fantasy and became a scientific possibility. Indeed, the driving force behind most of the field of exoplanet research is the discovery of habitable exoplanets and life.

The first extra-solar gas giants were discovered from 1995 onward (Mayor et al., 1995). These planets being hot, close-in Jupiter-sized planets means that they are relatively easy to identify. In fact, these planets could have been found decades earlier had they been specifically targeted (Struve, 1952). This does not hold for rocky planets. Since the advent of exoplanet research in 1995, the expanding exoplanet community has laid continuous focus on developing new methods and instruments to find smaller and colder planets, with the end goal of finding worlds which resemble the Earth in terms of size, mass and surface conditions. Both space-based and ground-based facilities have been employed to this end, culminating in tremendously successful programs like the Kepler and CoRoT observatories from space, and many surveys and observations from the ground. Although these initiatives are continuing to provide stunning discoveries of planets which may possibly be hospitable to life as we know it, the actual characterization of exoplanets and their atmospheres is still in its infancy. In fact, arriving at meaningful conclusions about the general composition and temperature-pressure structures of the biggest and hottest targets is already proving to be a very difficult task. Over the past decade, several attempts at constraining the nature of the atmospheres of some hot-Jupiters have resulted in success, but in the case of rocky exoplanets which are much harder to detect, conclusive results are scarce. It is becoming clear to the scientific community that although we are in the process of acquiring the ability to find the planets which may be capable of harboring life, actually assessing their habitability or finding indications of life on them will require continued progress for years or decades to come.

1.2 Exoplanet observations and habitability

Currently, the most successful method of studying an exoplanet is the combined use of radial velocity measurements and transit observations. Because the planet exerts a gravitational force on its host star, the star moves along a narrow orbit, which induces a measurable radial velocity oscillation which depends on the mass m_p of the planet and the orientation $\sin(i)$ of the orbit. If the orbital plane happens to be aligned with our line of sight to the system, the planet will also eclipse the star (and be eclipsed by the star) once per orbital revolution. Together, radial velocity and transit data constrain the mass, size, density and orbit of the exoplanet and provide a good indication of its nature.

In-transit absorption spectra and 'day-side' spectra of reflected light provide clues about the nature of the exo-atmosphere and the albedo of the planet. Compounds like sodium, methane, CO and CO_2 (see e.g. (Swain et al., 2009; Fossati et al., 2010; Snellen et al., 2010)) have been detected using space and ground-based facilities and in some cases, even rudimentary temperature maps of the planet can be made (Fujii and Kawahara, 2012; Majeau et al., 2012). Considering the fact that these planets are usually more than tens of parsecs away, the achievements of this young field are praised as a revolution in astronomy. However, we have only taken the first small steps in characterizing the worlds around us and the challenge at hand is a formidable one.

With the advent of space exploration in the 1960's, we gained the ability to visit some solar system bodies and study them in detail. Remote observations and (often robotic) in-situ measurements have given us a relatively deep understanding about the nature of our closest neighbors. We have the ability to see and map the planets, determine their composition, structure, surface conditions, atmospheric processes, geological and formation history, etc. Spaceflight has also enabled us to look at our own planet, showing us that the Earth is as complex a system as any other planet.

On Earth, geological, atmospheric and biological processes together have led to an evolving equilibrium in which life can be sustained over geological timescales. One example of such processes is the greenhouse effect which is regulated by the carbon cycle. Atmospheric CO_2 absorbs thermal radiation from the Earth's surface, and thereby acts to keep the surface temperature at an increased level. The rapid exchange between gaseous CO_2 and surface reservoirs (the most important of these being the oceans), causes a negative feedback loop between surface temperature and atmospheric CO_2 concentration. This process has the effect of a thermostat which has kept temperatures on Earth relatively stable for the past 0.5 Gyr (Falkowski et al., 2000). Another example of one of such processes is organic photosynthesis which has led to the presence of a large amount of molecular oxygen in the atmosphere. Without the presence of life (which is responsible for most of the oxygenation and respiration cycles), the Earth's atmospheric oxygen would be lost to chemical and surface reactions on timescales of 10^6 years (Duursma and Boisson, 1994). The atmosphere is said to be in *chemical disequilibruim*: Without organic processes, the Earth's surface would quickly reach a lifeless state. Therefore, the presence of molecular oxygen is a direct indicator for photosynthesis and life, which is why it is an important target in exoplanet studies.

A perhaps more important biomarker than oxygen is liquid water. Classically, the area in a stellar system at which the effective temperature of a black-body lies between the freezing and boiling points of water, is referred to as the habitable zone: The region in which surface water can supposedly exist in liquid form. In reality however, due to processes like the greenhouse effect, the conditions on a planets' surface can deviate significantly from what would be expected from black-body behaviour. Until the 1950's, the temperature at Venus' surface was thought to be similar to that of Earth (Venus being at the inner edge of the Sun's habitable zone). However, due to its thick CO_2 dominated atmosphere, the surface temperature is actually over 700 K owing to a runaway greenhouse effect (Mayer et al., 1958). The reason for this confusion regarding our closest neighbouring planet persisting into the second half of the 20th century, is the fact that Venus's clouds hide the surface, so unconventional measurements were needed to measure Venus' surface environment. In the case of exoplanets, situations like this will be very hard to identify because exoplanets can't be studied in nearly as much detail as the planets in the solar system. For instance because of the distances involved, any signatures we receive from exoplanets are generally disk-integrated, so there is no spatial information and in-situ measurements are not possible.

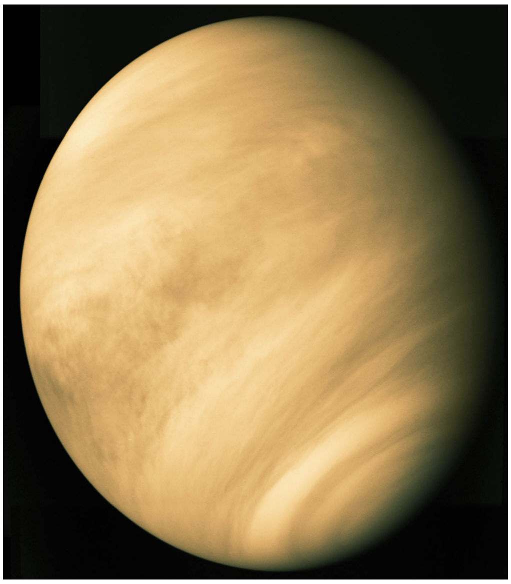

Figure 1.1: Until the 1950s, Venus's thick atmosphere was believed to hide a habitable surface environment. We now know that a runaway greenhouse effect has caused surface temperatures to be so high that the surface of Venus is one of the most inhospitable places in the solar system. The outward appearance of a planet, judging from spectral observations and basic assumptions about habitability, can be very misleading. Credit: Calvin J. Hamilton.

Figure 1.2 shows transmission spectrophotometry from transiting exoplanet Wasp-12b in the mid-IR. The solid lines are attempted fits of model atmospheres of different compositions. The figure serves to show that there is a lot of confusion regarding the nature of this planet, and many planets like it (see e.g. (Fraine et al., 2013)). Since these targets are not even nearly as small as the rocky planets we're interested in, and since the habitability of a planet is governed by many different processes, a great leap forward is required in the observing techniques of exoplanets. This is why we wish to turn to spectropolarimetry to extract more important information from the faint light we receive from exoplanets.

1.3 Polarization

Light emitted by a star is generated by thermal electrons in the photosphere. Because their thermal motions are random (i.e. have no preferential direction), the oscillation directions of all electromagnetic waves emanating from the star are essentially uniformly randomly distributed. The starlight is said to be *unpolarized*. However, when the electromagnetic wave experiences an asymmetrical interaction, a certain polarization direction will be preferentially selected and a change in the polarization state of the light occurs. This is the case in scattering/reflection events (in which the propagation direction is changed, see figure 1.3) and in polarization optics (which may feature different refractive indices or transmission coefficients for different polarization directions). Which polarization state is induced depends on the configuration of the scattering interaction and the properties of the material off of which the light is scattered.

The classical way to describe the polarization state of a beam of light (as opposed to the polarization state of an electromagnetic wave) is the *Stokes formalism* in which light is represented by a 4-element vector $\vec{F} = [I, Q, U, V]$ where Q and U represent the amount of linear polarization in two directions and V the amount of circular polarization, either clockwise (left-handed) or counter-clockwise (righthanded, see figure 1.4). We define the

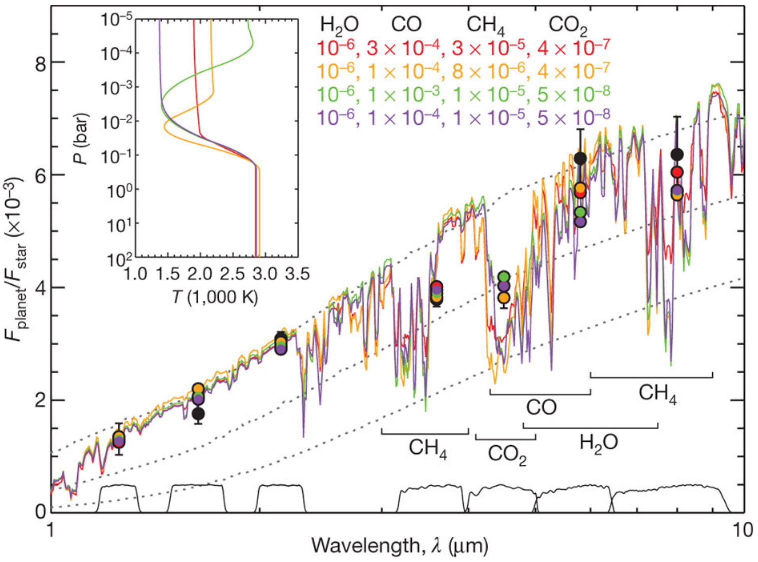

Figure 1.2: Spectrophotometric measurements of transiting hot-Jupiter Wasp-12b adopted from Madhusudhan et al. (2011). The circles indicate the measurement values, while the various coloured lines are fits to the transmission spectrum, of model atmospheres with different compositions. Spectral measurements like these are confusion limited, and it is thus hard to constrain the global composition of an exoplanet atmosphere using purely spectral measurements, let alone other environmental parameters.

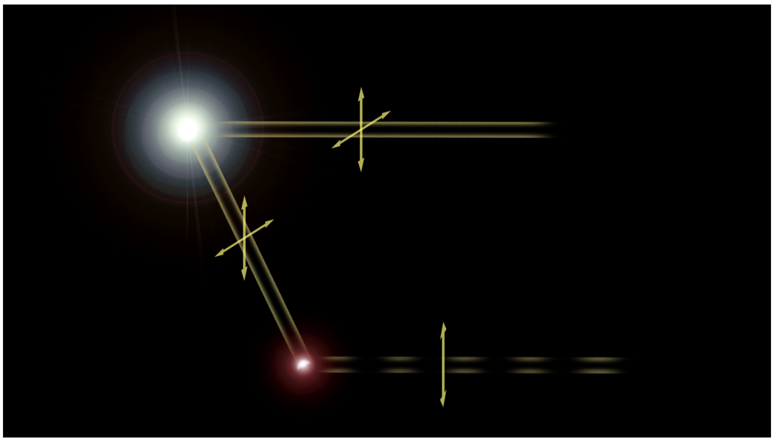

Figure 1.3: Upon scattering off of an exoplanet's surface, unpolarized starlight will be partially polarized. By selecting for the right polarization direction, unpolarized starlight can be suppressed and the contrast between the star and the planet can be increased. The spectropolarimetric profile of the scattered starlight depends on the properties of the scattering material on the planet's surface and in the planet's atmosphere.

degree of linear polarization P_L and the *degree of circular polarization* P_C as the fraction of the flux which is polarized with respect to the total flux:

$$P_L = \frac{\sqrt{Q^2 + U^2}}{I}$$

$$P_C = \frac{V}{I}$$

Also, we define the *angle of linear polarization* as:

$$\phi_L = \frac{1}{2} \arctan \frac{Q}{U}$$

As outlined earlier, $\vec{F}$ is a function of wavelength λ and depends on the scattering angles and the material properties of the scatterers involved. It is this wavelength dependence which we wish to characterize in order to take the next step in exoplanet characterization.

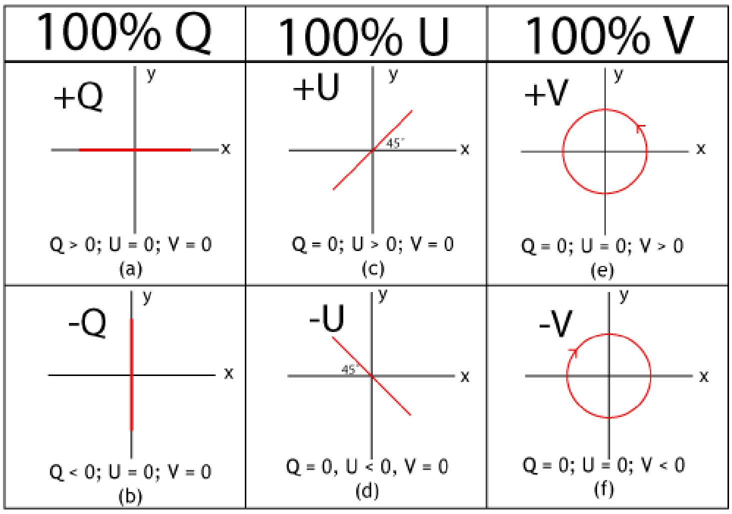

Figure 1.4: Visualization of the three Stokes parameters. Credit: Dan Moulton.

Because the light scattered off of a planet will pick up a certain polarization, selecting that polarization state with a polarimeter suppresses the unpolarized starlight when attempting to directly observe the exoplanet. The polarimeter acts as a pass-filter for the light coming from the exoplanet and thus enhances the contrast between the planet and the host star. The fact that an exoplanet is outshined by its host star by orders of magnitude severely limits the direct detection of exoplanets, and contrast-enhancing techniques are especially vital to directly observe the cooler and smaller ones. Also, the polarization being dependent on the configuration of the system, a polarization measurement of the planet helps to confirm that the observed object is in fact a planet, without the need for followup observations later in the orbit.

There are also other reasons why polarization measurements of exoplanets are important. The material properties of the scattering material have a great influence on the polarization state of the scattered light. For example, scattering of starlight off of a cloud of aerosols will induce a certain polarization state, depending on the scattering geometry, but also on the microscopic properties of the aerosols. In fact, in the case of climate research, polarization information is essential to determine the properties of the different types of aerosols in the Earth's atmosphere (Mishchenko et al., 2007; Mishchenko and Glory APS Science Team, 2011). However, polarization is not only useful in the case of detailed climate studies like the ones we can do on Earth and in the solar system, but also when constraining the basic properties of exoplanets, using the disk-integrated light which we receive from their dayside surface.

Figure 1.5 shows plots of the reflected intensity πF_n and degree of linear polarization P_L of a radiative transfer model of Earth (Stam, 2008). The left panels show the disk-integrated spectral and spectropolarimetric profiles for cases where different surface types are in view. Although a fully-clouded Earth features a well distinguishable (mostly flat) spectral profile, the difference between oceans and landmasses is much harder to identify from spectra alone. The only major deviation between the two spectra stems from the 'red edge' beyond 700 nm, for which vegetation is responsible. Had the Earth been free of plantlife, the two surface types would be hardly discernible. However, if we take knowledge about P_L into account, this degeneracy is broken, as the difference between oceans and landmasses can clearly be seen in the lower-left panel. In addition, globally induced polarization at a single-wavelength also contains a wealth of information. In the right panels of figure 1.5 similar simulations are plotted, showing the variation of disk-integrated intensity πF_n and polarization P_L as a function of planetary phase at a wavelenght of 550 nm. The high-frequency oscillation is caused by the day-night cycle of the Earth and is very well detectable. Around 30° phase angle, P_L shows a rapid increase which is caused by scattering of sunlight off of water droplets in the atmosphere. The same scattering process is responsible for the rainbow effect and is believed to be a unique indicator for the presence of liquid water droplets in the atmospheres of exoplanets (Stam, 2008). These models serve to show that on a global scale, polarization measurements will contain information complementary to intensity measurements. By using polarisation, we can thus eliminate confusion between different types of surface material or different phases of the same material, which would otherwise limit our understanding of exoplanet observations (Stam, 2008; Karalidi and Stam, 2012).

Finally, biological compounds are known to exhibit *homochirality*: The preferential occurrence of a certain configuration of the molecule. Many basic biological compounds (like amino acids and nucleic acids) only occur in one chiral form and although the reasons for this are poorly understood, it is believed that homochirality is a necessary attribute of the information-replicating processes which make life possible and that it may even be a defining aspect of life itself (Carroll, 2009). As indicated earlier, the material properties of a scatterer determine the polarization effect which it induces upon illumination. The preferential occurrence of a certain configuration of asymmetric molecules is therefore expected to induce a macroscopic polarization state. It was shown by Sparks et al. (2009) that photosynthetic microbes and vegetation induce circular polarization upon reflection. Although some aerosols are known to produce circular polarization as well, the spectral properties of homochiral compounds is so distinctive that circular polarization can be concluded to be a powerful biomarker.

1.4 Earth Observations

The first step in finding living or habitable worlds is to define what we consider to be 'life'. Earth alone hosts a great variety of lifeforms, some of which are living under extreme thermal, pressure and chemical circumstances. Considering the diversity of planets that have been discovered thus far, we may expect that any alien life we would find is of a very different nature than terrestrial life. However, there is little knowledge about the forms in which life may possibly exist, and thus what the constraints on habitability really are. Also, any measurements containing the signatures of an unknown form of life may be difficult to correctly interpret. When performing any grand searches for habitable worlds, we are therefore compelled to target exoplanets which resemble the Earth, because the Earth is the only habitable planet which we can study in any sorts of detail. Therefore, we need to have a thorough understanding of what the Earth would look like from afar, i.e. which biomarkers are discernible from the disk-integrated spectropolarimetric profiles and how that depends on different observing conditions.

Earthshine

A possible way to perform Earth-observations is to look for *Earth-shine* which is reflected from the dark side of the Moon. Measurements like these have been attempted for the purpose of finding the polarization spectrum of Earth. However, such measurements are

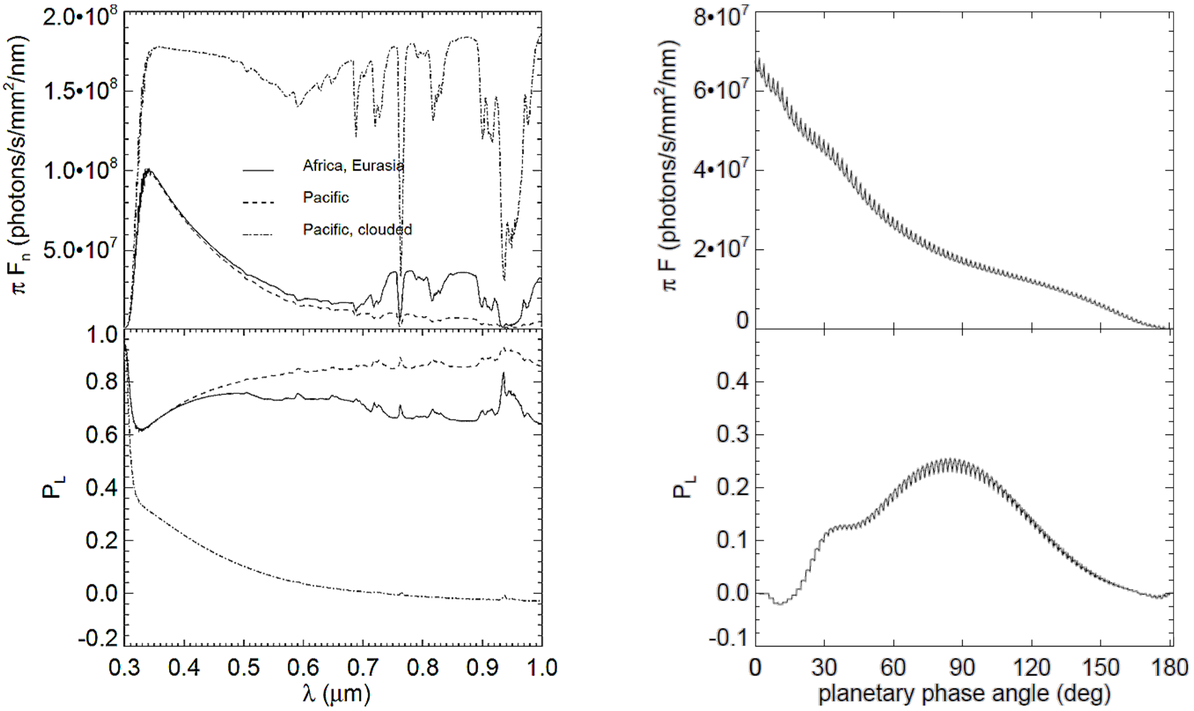

Figure 1.5: These plots show simulations of the polarization behaviour of a model of planet Earth. The models are built up by combining the calculated polarization spectra of four different planets, each covered totally with either sand, forest, oceans or ice, to represent the surface distribution of landmasses on Earth for different phases. The left panels show the intensity spectrum I (up) and polarization spectrum P_L (down) for when Africa and Eurasia are in view, when the pacific is in view, and when the disk is fully clouded. Note that although clouds stand out in the intensity spectrum, different surface types produce a very similar spectrum, especially considering the fact that the feature from 700 to 900 nm is caused purely by vegetation. In the polarization spectrum however, these profiles are clearly distinguishable. Small features arise in the spectra due to absorption features. An important one of these is the feature at 760 nm due to O_2, which is visible both in polarization and in intensity. The right panels show the disk-integrated intensity and degree of polarization at a wavelength of 550 nm, for different phase angles and a cloud coverage of 42%. At 0° phase, the entire disk is in view and the received intensity is maximum. The polarization peaks at 90° or 'half-Earth', and shows an enhancement around 30° phase, which is caused by single scattering off of water droplets. This enhancement is also visible in the intensity spectrum, but it is much less pronounced. This underlines the usefulness of polarization when searching for biomarkers, such as atmospheric water. For more details about these models, see (Karalidi et al., 2012).

difficult because the reflection off of the lunar surface has a de-polarizing effect on the polarized Earthshine. This induces systematic errors which are not well understood. Sterzik et al. (2012) measured the polarization of Earthshine, using the FORS spectrograph at the VLT in April and June, 2011 (see figure 1.6). The authors compare their results with the models presented by Stam (2008), after scaling them with an assumed de-polarization factor due to the lunar surface, which they acknowledge is not well-determined. Interestingly, a clear feature due to Oxygen is visible in these measurements around 760 nm, as well indications of the vegetation which covers much of the Earth's landmasses. Their observations however, are not fully accounted for by the models presented by Stam (2008), hence their call for more advanced radiative transfer models and for independent validation of such models.

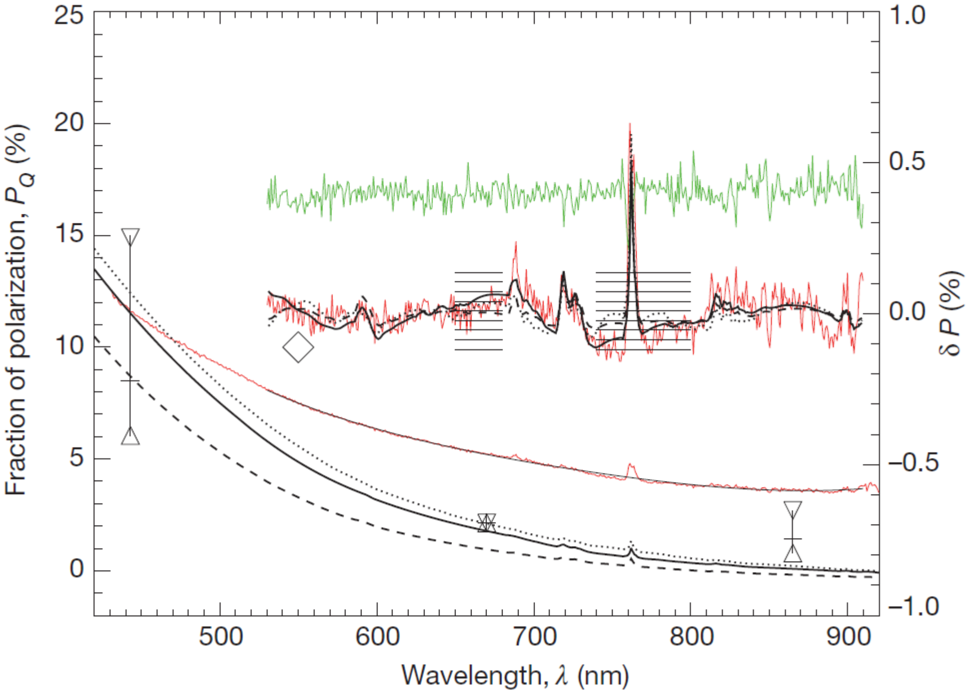

Figure 1.6: Polarization spectrum of Earthshine, measured by Sterzik et al. (2012) on april 25, 2011. The authors plot only the Q component as the degree of linear polarization, because the instrument was oriented such that U is zero. The red line is the measured spectrum of P_Q, while the black lines towards lower values of P_Q are models based on the modelling scheme presented in (Stam, 2008), on which the models of (Karalidi et al., 2012) are also based. The right vertical axis measures a zoom-in of the relative value of P_Q between 530 and 910 nm, after dividing with a 4^{th} order polynomial to remove the continuum. This clearly shows the increased degree of polarization of the O_2A feature. The green line denotes measurements of P_U. Because P_U is expected to be zero, a measurement of P_U is equivalent to a noise-measurement. Finally, the triangles represent POLDER data for low or high cloud levels, at 443, 670 and 865 nm. In order to account for lunar depolarization effects, the authors reduce the modelled values for P_Q (black curves) with a depolarization term which is linear in wavelength depol $= 3.3\lambda/(550\text{ nm})$.

Bazzon et al. (2013) attempted to correct the lunar de-polarization in their broadband Earthshine observations by referring to studies of the back-scattering behavior of lunar samples brought back by astronauts from different regions of the Moon, as a function of wavelength and scattering angle (Hapke et al., 1993, 1998; Velikodsky et al., 2011). They obtain disk-integrated linear polarization phase curves of Earth, which are in good agreement with the models presented by Stam (2008) (see figure 1.7). However, attempting to reconstruct the global polarization behavior of the lunar surface in this way seems questionable. If this approach would be robust, Earthshine observations would not be necessary in the first place, because we could simply reconstruct the Earth's polarization spectrum by studying the scattering and reflection behaviour of different types of sands, rocks, ices, clouds, forests, seas and oceans, without having to turn to the sky. Another severe limitation of Earth-shine measurements are the cadence and the coverage: The measurements include only the hemisphere on which the telescope is situated and observations can not be performed when the position of the Moon in the sky is not favorable, or when the Moon is not in the sky at all. Therefore, a different Earth-observing approach is warranted.

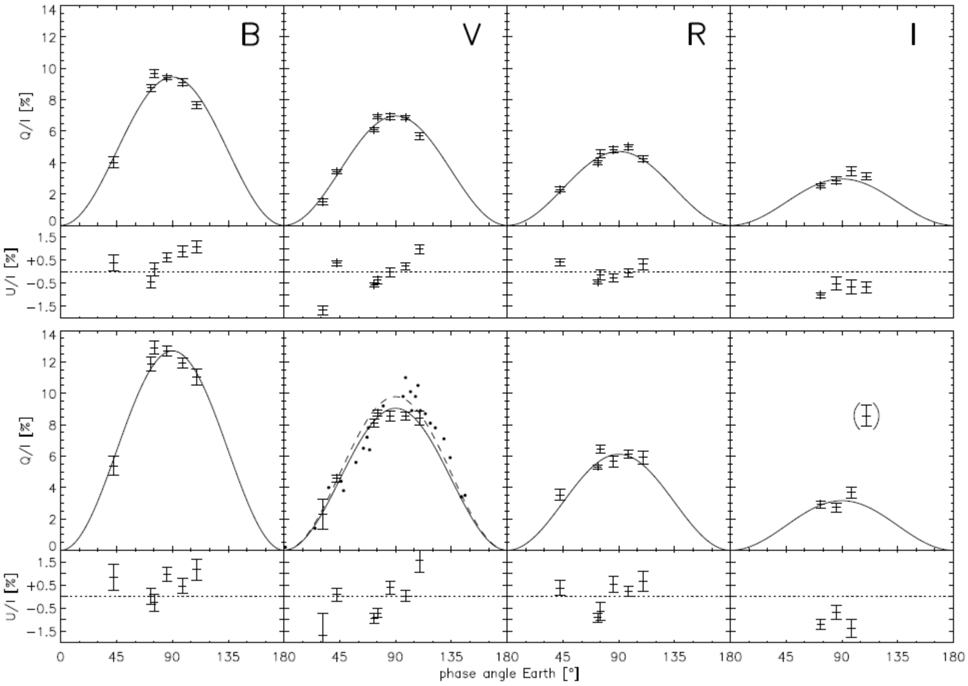

Figure 1.7: These plots from Bazzon et al. (2013) show phase curves obtained by observing Earth-shine reflected by highland (top) and mare (bottom) regions on the moon using the ESPOL instrument in four different filters. $\sin^2$ profiles are fit to the phasecurves, which confirm the behavior of the modeled profiles presented by Karalidi et al. (2012). These phasecurves are subsequently corrected for lunar depolarization (not shown) by a log-linear relation which they derive from the backscattering properties of a collection of lunar samples. Although the characterization of errors and systematics in this work is extensive, the author acknowledges that the spectral and temporal resolution of these measurements leaves to be desired.

Earth-observing satellites

Over the past decades, numerous Earth-observing satellites have been deployed to monitor the Earth's surface, weather and climate. Such probes are usually placed in low-earth orbit because that enables them to scan the Earth's surface below in detail. One of these is the PARASOL micro-satellite, carrying the POLDER imaging polarimeter. Three of POLDERs nine spectral bands provide polarization imaging capability which are used to create maps of the aerosol load in the Earth's atmosphere (see figure 1.8).

Measurements like these are useful for applications in which spatial detail is needed, but not when disk-integrated observations are required because the field of view required for such observations would be close to 180°. The synthesis of a global measurement from many independent observations of different regions, does not provide a measurement which is representative of the entire disk at any given instance, so for instantaneous disk-integrated measurements a wide orbit is required. In orbits which are close to geostationary, the field of view required to capture the entire Earth's disk is 24°, but GEO is designed such that the same hemisphere is in view all the time. Any orbits slightly deviating from GEO therefore require long lifetimes to fill the parameter space of phase angles and diurnal cycles. See figure 1.9 for a schematic comparison of Earth-shine and LEO observation configurations.

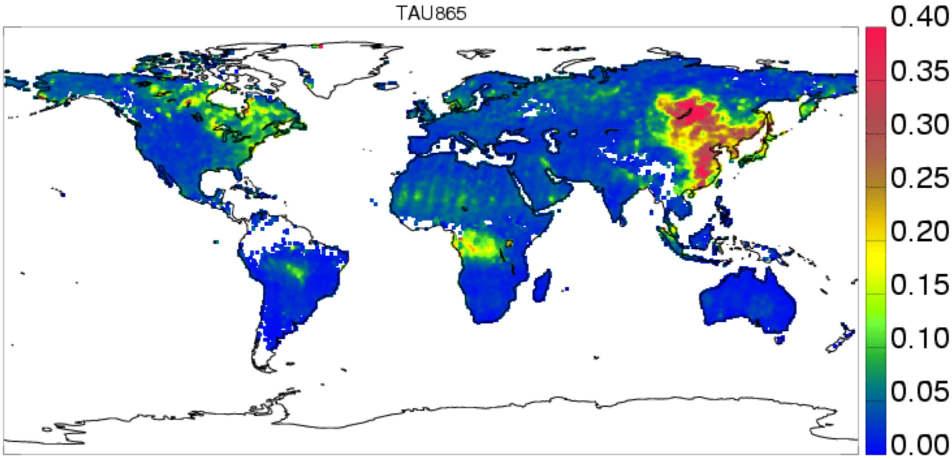

Figure 1.8: Synthesis of images taken by the POLDER instrument during June 2003 of the aerosol optical thickness at a wavelength of 865 nm. This image was constructed from measurements taken along many subsequent orbits, so the optical thickness at each image pixel is an average of many exposures. This reflects the fact that orbital instruments like POLDER are unable to provide any polarization maps of the entire Earth at any given instant in time.

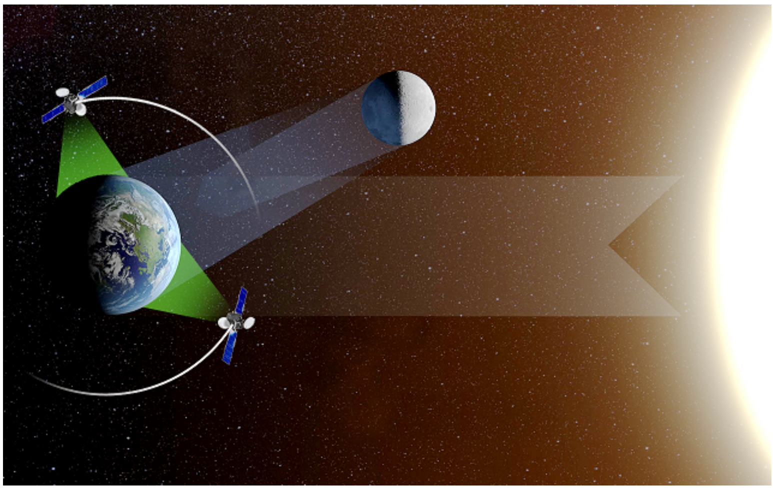

Figure 1.9: Comparison of Earth-observations through Earthshine measurements and instruments aboard satellites. Earth-shine observations suffer from partially unknown systematics related to the scattering properties of the lunar material, the scattering geometry and the cadence of the observations is low because they can only be performed at certain times in the month. Also, observations from a single observatory are necessarily limited to cover the Earth-shine from a single hemisphere. Typical satellite orbits are also not suitable for these global observations, because from a low Earth orbit it is impossible to capture the entire Earth's disk in a single observation. From orbits close to GEO, long mission lifetimes are needed to fully cover the ranges of illumination angles and diurnal phases. Credit: ESO/L.Caada.

1.5 LOUPE

In contrast to satellites, the Moon offers a suitable observing platform. The lunar orbit is such that all diurnal phases of Earth are covered roughly every 24 hours, while all phase angles are covered once per month. Because of tidal locking, the same hemisphere of the moon always faces the Earth which means that from the Earth-facing lunar surface, the Earth is always in the sky, ensuring 100% visibility. Interestingly, several lunar landing missions are envisioned to take place over the course of the next few years, which makes an appealing case to combine the effort of this observing program with a larger lunar mission. Such a cooperation would eliminate the need to build a dedicated orbital platform for these observations. Therefore, Karalidi et al. (2012) proposed LOUPE: The *Lunar Observatory for Unresolved Polarimetry of Earth.* This thesis describes the design and construction of a prototype, building from the science case outlined by Karalidi et al. (2012) and the measurement principle presented by Snik et al. (2009). The second chapter describes and expands on the science goals and instrumental requirements of the instrument. The third chapter describes the design of the prototype setup and is followed by a chapter describing the implementation in detail. The final two chapters present an analysis of the performance and some concluding remarks for further development of the instrument in the future.

Chapter 2

Science goals and instrument requirements

2.1 Implementation avenues

The scientific goal of LOUPE is to quantitatively validate radiative transfer simulations of exoplanets, of the kind presented by Karalidi et al. (2012) and Stam (2008). Direct observations of exoplanets can be performed at arbitrary orbital phase, and arbitrary surface regions may be in view. Therefore, the observing conditions of LOUPE must be such that the entire parameter space of different viewpoints be filled during the lifetime of the instrument. This means that LOUPE should observe the Earth across all phase angles and diurnal phases, so that all areas on the Earth are observed under all illumination angles. Also, it is possible that the global spectropolarimetric profile changes with seasonal variations of global weather. Although these variations might small, and thus not bear much direct significance in the context of exoplanet research, such measurements can be extremely useful for the field of climate research, because no global, long-period polarimetric observations of the Earth exist yet.

In order to further mimic future exoplanet observations, these measurements should be disk-integrated, as exoplanet detections are unresolved. Somewhere within the hardware or the pipeline, the light from the entire Earth's disk should thus be combined into a single spectropolarimetric measurement. The notion that the measurements should be disk-integrated does not exclude the possibility of maintaining spatial information. It is possible to construct a form of imaging spectropolarimeter which analyses light from different regions on Earth separately, before combining all of the light into a single spectropolarimetric profile. Similarly, it is possible to not only measure the linear polarization spectrum, but the circular polarization spectrum as well (Sparks et al., 2012). We thus have four fundamentally different possible implementations of the instrument, which were termed *LOUPE-1A, 1B, 2A* and *2B* by Karalidi et al. (2012). LOUPE-1A and 1B do not preserve spatial information and measure only linear polarization (1A) or the entire stokes vector (1B). Conversely, LOUPE-2A and 2B do preserve spatial information. It is clear that LOUPE-2B is the most challenging to develop.

In this project, we attempt to construct an instrument which measures only linear polarization, with or without spatial resolution (1A, 1B). The addition of circular polarization is expected to greatly increase the complexity of the device. Global circular polarization signatures are expected to be of the order of 10^{-4}, which are thus two orders magnitude fainter than typical linear polarization signatures (Sparks et al., 2012). Distinguishing the two will be challenging, because a mere 1% of cross-talk from linear to circular polarization (for example through aberrations in the objective lens) would overwhelm the circular component present in the source. Also because circular polarization signatures are expected to be very faint, circular polarization is not likely to find any applications in the field of exoplanet research for many more decades to come.

In the following sections, quantitative requirements relating to the most important aspects of the case outlined above will be derived.

2.2 Spectropolarimetric properties

Three factors describe the quality of the measured spectropolarimetric data. The first of these is the *resolution* which is determined by the size of each wavelength interval in which the polarization state is measured. This is analogous to the notion of spectral resolution in an ordinary spectrograph.

The second is *sensitivity* which is determined by the random noise in each polarization measurement and which limits the detectability of the source polarization. A sensitivity of 1% means that polarization variations exceeding 1% can be detected, while variations which are smaller than that are indistinguishable from noise. If the source is bright (as is the case in this application, see section 3.2), the noise in the polarization measurement is dominated by counting noise in photo-electrons, which scales with the inverse of the square root of the number of incoming photons.

The last qualifier is the *accuracy* of the measurement, i.e. how close the measured polarization signal is to real input polarization. The optics in the instrument may induce spurious polarization signals and/or cross-talk from one polarization state to another. The accuracy of the final polarization measurement are therefore limited by how well these systematics can be calibrated for.

Figure 1.5 shows the expected profiles of the intensity and degree of linear polarization of sunlight scattered off of Earth. The variations are generally larger than $\sim 0.1\%$ and mostly occur over scales larger than ~ 20 nm. The spectropolarimetric resolution and sensitivity should match these (Karalidi et al., 2012). An absolute accuracy of 1% is needed to determine the exact phase angle at which the polarization is zero. The zero-crossing of the phase curve depends on the configuration of cloud particles in the atmosphere, which is an important parameter to characterize. Also, a reliable comparison between polarization spectra at different phase angles requires the measurements of P_L to be absolutely calibrated. The greatest challenge is that the accuracy should be stable in time, which is an issue which will again be referred to later.

2.3 Cadence and Field of view

In order to see the entire Earth's disk, the instrument should have an acceptance angle of at least 2°, as the angular diameter of the Earth is 2° as seen from the Moon. Due to the ellipticity of the lunar orbit however, the Earth does not appear to be stationary in the sky, but it is said to *librate*. Over the course of one month, it oscillates across the sky with an amplitude of roughly 9°. Figure 2.1 shows the path the center of the Earth's disk appears to follow over the course of one lunar orbit. To sample all diurnal phases and phase angles, the instrument should be able to observe the Earth at all times. To accommodate this, the instrument should either feature a large field of view or it should be pointed actively to track the Earth continuously. The ability to track would require motion around at least 2 axes and this would pose a severe increase of complexity which is undesirable in space instruments. Therefore, we explore a design in which the instrument is assumed to be pointed towards Earth coarsely after landing on the lunar surface. Under the assumption of a single pointing, if the FOV were to be less than $20^\circ \times 20^\circ$ the Earth would move out of view during certain times in every month. This would render certain orbital phases systematically unobservable unless the lifetime of the instrument were to be of the order of one year. This is even more problematic if the parameter space is to be sampled more than once. We assume no such lifetime and therefore require that the FOV encompasses the entire libration curve, 20° × 20°.

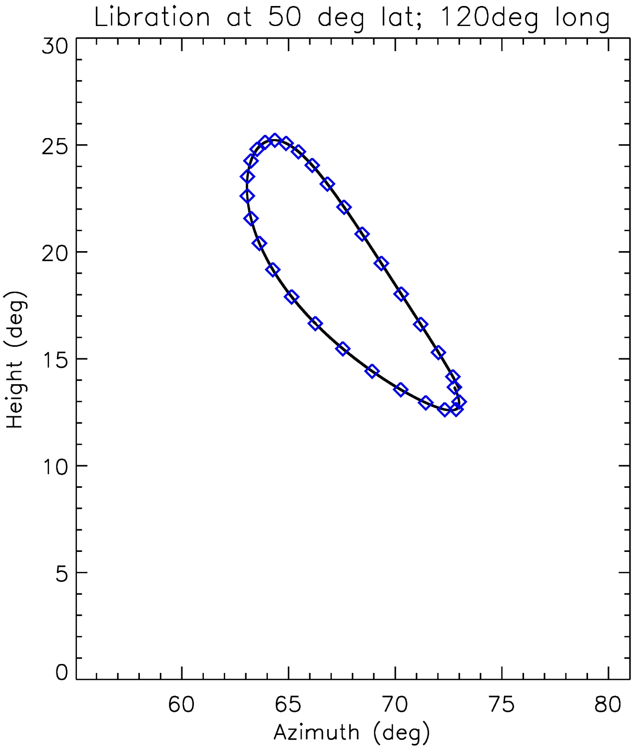

Figure 2.1: Simulations of the apparent motion of the Earth on the lunar sky, caused by the ellipcital orbital motion of the Moon around the Earth. The diamonds indicate the position of the center of the Earth's disk. The lunar meridian is taken to be the semi-circle passing through the points on the lunar sphere which are closest and furthest away from the Earth at $t = 0$, with increasing longitude in the eastern direction. The extent of the libration curve is roughly 18°. Including the angular diameter of the Earth (2°), the Earth is seen to cover an area of 20° wide over the course of one month. This simulation takes into account only the ellipticity of the orbit. Other orbital effects (like perturbations caused by the Sun) do not significantly alter this apparent motion and are therefore ignored.

2.4 Spatial resolution

Although the end-result of the observations is a set of disk-integrated spectropolarimetric profiles, information about the spatial structure of the polarization signal can be maintained by incorporating a form of imaging spectroscopy in the design. To do this, the field is to be sliced into smaller areas onto each of which spectropolarimetry can be performed separately. In this way, the influence of different surface types on the global signal can be disentangled. Such measurements will clarify which signatures are indicative of important surface features such as liquid water and vegetation and can provide important constraints on polarization models. The largest variations in surface type are of continental scale. We therefore require the spatial resolution of the spectropolarimetry to be better than $\sim 0.4°$, which amounts to 2500 km × 2500 km at the equator and 5 spatial samples across the disk. The FOV measuring 20°, will then consist of 50 × 50 spatial elements, only a few of which being occupied by the Earth at any given time.

2.5 Oxygen A - band

One of the major absorbers in the Earth's spectrum is an absorption by oxygen. The most prominent absorption feature is a band near 760 nm which is dubbed the O_2A band. This absorption signature is well visible in the polarization spectrum (see figure 1.6) and it's polarization strength is dependent on the oxygen abundance in the atmosphere and the top of the cloud layer (Sterzik et al., 2012). Combined with the fact that oxygen is considered to be a biomarker, this feature at 760 nm is an important target for LOUPE. We require the spectral resolution of the instrument to be sufficient to resolve the O_2A band, which has a width of 7.5 nm (Karalidi et al., 2012; Brown, 2000).

2.6 Radiometry

A major unknown in the great debate surrounding global climate change and the greenhouse effect is the absolute value of the disk-integrated albedo of Earth. Assuming a constant effective temperature T_{eff}, solar irradiance S and disk-averaged albedo α, the global energy balance of Earth must satisfy:

$$\pi R^2 S(1-\alpha) = 4\pi R^2 \sigma T_{\text{eff}}^4$$

.

The albedo thus is a determining factor in the global climate. Variations or errors in the determination of the albedo can give rise to gross misinterpretations of the climate issue. Several studies have been performed, comparing albedo measurements of radiometers aboard orbital satellites (such as ERBE and the CERES constellation) with those of climate models. Not only do they find significant systematic differences between the models and the satellite data, the satellites are not in agreement with each-other either (Bender et al., 2006; Kim and Ramanathan, 2012). The authors attribute these inconsistencies to the fact that global signals derived from the synthesis of many localized observations critically suffer from low cadence combined with a transient environment. In fact, even the choice of data processing algorithm can severely impact the measurements.

The models investigated by Bender et al. (2006) indicate that disk-averaged albedos range betwee 0.294 to 0.319, while the satellites indicate albedos of 0.2942 ± 0.006 (ERBE) and 0.282 ± 0.003 (CERES). On average, these deviations correspond to 3.3 Wm^{-2} and 6.8 Wm^{-2} in net outgoing short wave radiation, compared with the mean of the modeled albedos. In contrast, radiation forcing due to anthropogenic greenhouse gases only amounts to 2.4 Wm^{-2} (IPC, 2001), which means that these uncertainties in our knowledge of the Earth's albedo fundamentally limit our understanding of the climate problem. Without more robust albedo measurements, mankind's contribution to the warming of our atmosphere is severely obfuscated.

LOUPE is to circumvent the need for synthetic polarimertric observations from low orbit by going to the Moon. Clearly however, the problem of retrieving the disk-integrated albedo of Earth is fully analogous. Therefore, the added capability of performing radiometric measurements of Earth from LOUPE's vantage point would be highly meritorious. The albedo anomaly between the ERBE and CERES satellites and the models investigated by Bender et al. (2006), amounts to $0.01 - 0.02$, or $3.4\% - 6.8\%$. To suppress the resulting uncertainties in radiative forcing below that of greenhouse gases, an improvement in the accuracy of the mean global albedo of roughly an order of magnitude is needed. In order to meet this demand, radiometric measurements performed by LOUPE should thus have an accuracy of approximately 0.5%.

2.7 General considerations

LOUPE being a space instrument, it is subjected to a multitude of additional requirements. The most important constraint of any space instrument is that it should be small in terms of physical dimensions and weight. Whereas on ground-based instruments, size and mass usually don't pose stringent limitations on the design, the functionality of space instruments is often fully determined by size and mass considerations. Especially because LOUPE is aimed to be added to the lander of a third party, the impact which LOUPE would have on the mass budget of this mission should be minute. Also, it is important that the instrument is not complex. Moving parts are expensive prone to failure, and usually limit the lifetime of any mission if continuous or repeated mechanical movement is needed for sustained operation of the instrument. If possible, LOUPE should therefore be completely solid-state.

Data transfer is another important factor in space mission design. Communication with remote instruments requires large antennas and power supplies. Since LOUPE will perform many measurements at regular intervals, care must be taken to limit the amount of gathered data to pure necessity.

Calibration of the instrument should be performed either on the ground, before the mission, or in-situ. In-situ calibration requires additional systems which add to the complexity of the instrument, while pre-flight calibration is more risky because then, the accuracy of the observations can never be determined independently during the mission.

Finally, space instruments have to survive extreme environments. They must be able to withstand the rigours of launch and the harsh space environment. Specifically, LOUPE should be able to function continuously across a wide range of temperatures, as the temperature on the lunar surface varies by hundreds of degrees depending on whether the lander receives direct sunlight or not. Snik et al. (2009) developed a design framework for a-thermalizing the retardance of the optical crystal used in this measurement principle (see section 3.1). An a-thermal response is an essential requirement the operation of the instrument, unless the temperature could be measured and calibrated for, but this would add considerable complexity. Also, during certain times of the Month, the Sun will be in the FOV. Care must be taken that the instrument can withstand (or is protected against) direct irradiance by the Sun[1].

2.8 Summary

In summary, the science goal of LOUPE is the following: *'LOUPE shall perform disk-integrated spectropolarimetric measurements of the Earth across all diurnal cycles and phase angles. The observations shall span visible wavelengths and include spectrally resolved measurements of the O_2A band. If permissible, the observations shall characterize both linear and circular polarization spectra, preserve spatial resolution of the Earth's disk, cover all of Earth's seasons and perform absolute power measurements to characterize the Earth's albedo.'* (Karalidi et al., 2012). All top-level requirements following from this science case are summarized in the list below.

---

[1] It is conceivable that such a protective system would require the use of a moving shutter, or that the mission lifetime be limited to only a single month.

R1: Observations are disk-integrated.
In order to mimic exoplanet observations, all light of the Earth 's disk must be gathered and analysed as a single measurement.

R2: Observations cover all phase angles of Earth.
As the Moon orbits the Earth once a month, LOUPE will need one month of observations to cover all illumination angles, with a visibility of 100%. This requires a field of view of 20° by 20°.

R3: Observations cover all diurnal phases of Earth.
The exposure time of the observations is of the order of minutes, as to not be influenced by the Earth's diurnal rotation.

R4: Observations cover a bandwidth of 400 nm – 800 nm.
LOUPE targets reflected Sunlight, which peaks in the visible. This regime encompasses important features due to aerosols, water and oxygen.

R5: The O_2A band is spectrally resolved.
As the width of the O_2A band is 7.5 nm, the spectral resolution should be roughly 3 nmpx^{-1}.

R6: The spectropolarimetric resolution is 20 nm.

R7: The spectropolarimetric accuracy is 1%.

R8: The spectropolarimetric sensitivity is 0.1%.

R9: The spatial resolution is $0.4°$.
This allows for the spatial separation of continents-sized structures.

R10: The absolute flux of the irradiated Earthshine can be measured with an accuracy of $\sim 0.5\%$
This suppresses the systematics which are currently present in measurements of the mean global albedo of Earth by roughly an order of magnitude, and will alleviate uncertainties regarding the impact of greenhouse gas emission on global climatic stability.

R11: The instrument has a low impact on the design of the landing vehicle.
LOUPE shall have a low impact on the power, data, size and mass budgets of the mission with which it flies.

Chapter 3

Design concept

The basis for the design is the implementation of the SPEX setup, which will be introduced in the next section. After introducing SPEX, we first reconstruct it in it's most basic form in the lab (*LOUPE-1A* from section 2.1), after which we expand the setup to include the capability of imaging spectroscopy with the goal of matching spectral properties, as described in section 2.2.

3.1 Measurement principle: SPEX

Polarization measurements are widely known for suffering from considerable systematics. This is because in order to characterize the linear polarization state of a source, one needs to measure four polarization components: 0° and 90° for Q, and ±45° for U. Ordinarily, this is implemented by rotating a polarization optic (like a linear polarizer or a quarter wave plate in front of a fixed linear polarizer) in the beam and subsequently measuring the transmitted intensity at the four rotation angles. These measurements being performed independently at different times, the resulting values for I, Q and U will suffer from errors due to temporal effects like motion of the instrument (e.g. pointing or vibrations) or transience of the source. Alternatively, the beam might be split into four beams according to polarization direction, using optics like a polarizing beamsplitter, after which the intensity in each beam can be measured separately. To do this, part of the optics in the device needs to be duplicated, increasing the size and complexity of the instrument. Even through the beamsplitter allows the measurements to be obtained simultaneously, systematics are induced by differences between the optics in the different beams.

Snik et al. (2009) presented a way of encoding the polarization information in the wavelength dimension, rather than in time or space. This method makes use of the fact that the retardance of a birefringent crystal is a strong function of wavelength. If the instrument is designed to spectrally disperse the beam, the wavelength-dependence of the polarization optics will cause an intensity modulation to be imprinted onto the spectrum. The idea of imprinting polarization information in the spectral dimension was first proposed by Oka and Kato (1999) and Jones et al. (2004). Snik et al. (2009) presented a simplified version of this principle, in which only the linear polarization component is encoded into the spectrum. An important improvement in their design is that by layering different crystal materials, the birefringent optic can be made athermal across visible wavelengths, which is important in an extreme observing environment like the lunar surface.

The design features a sequence of an achromatic quarter-wave retarder, a multiple order retarder with retardance $\delta(\lambda, T)$ (in which the temperature dependence ideally is weak) and a linear polarizer. The transmission axis of the polarizer is aligned with either the fast or the slow axis of the quarter-wave plate, while the fast-axis of the multiple-order retarder is rotated by 45° with respect to the axes of the other two.

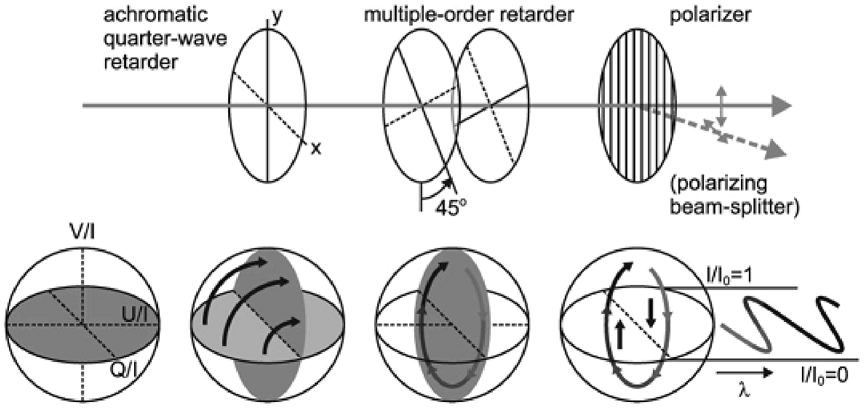

Figure 3.1: Schamatic of the SPEX principle. The lower panel shows the Pointcaré representation of the modulation mechanism. An achromatic quarter-wave retarder transforms linear polarization (Q,U) into partial circular polarization (Q, V). Depending on the retardance of the MOR (and thus the wavelength of the radiation), the Q-V-mixture picks up a phase rotation in the pointcaré representation. Finally, all V-components are filtered out by the linear polarizer, leaving only a sinusoidal intensity variation in Q, as a function of wavelength.(Snik et al., 2009)

This combination of optics imprints a sinusoidal intensity variation in the spectrum, following equation 3.1 This setup and the modulation principle are shown schematically in figure 3.1. .

$$S(\lambda) = \frac{1}{2}s_0(\lambda) \times \left[1 \pm P_L(\lambda)\cos\left(\frac{2\pi\delta(\lambda,T)}{\lambda} + 2\phi_L(\lambda)\right)\right] \tag{3.1}$$

Here, s_0 is the spectrum of the source, and the ± sign depends on whether the linear polarizer is aligned with the fast or the slow axis of the QWP. The orientation of the linear polarizer selects orthogonal polarization channels. On top of the spectrum s_0, the sinusoidal modulation is imprinted, which has an amplitude which scales with P_L and a phase which scales with ϕ_L. s_0 is recovered by averaging the two channels, while the spectral modulation itself is recovered by calculating the visibility:

$$V = \frac{I_1 - I_2}{I_1 + I_2}$$

By fitting a sinusoid to the modulation profile, the values of P_L and ϕ_L can be recovered. Generally, these will vary with wavelength, so the spectral range should be sliced into a number of bins, in each of which the modulation profile may be fitted. This is illustrated in figure 3.2. It is important to realize that because multiple spectral measurements are used per fit, the spectropolarimetric resolution will be significantly lower than the spectral resolution. The modulation scheme exchanges spectral resolution with spectropolarimetric resolution, although the original spectrum can be recovered in full resolution, when both channels are averaged.

The sensitivity of the spectropolarimetric measurement is determined by how well the amplitude of the spectral modulation (equation 3.1) can be determined by fitting. This is equivalent to measuring an intensity variation, meaning that the instrument needs to have a sensitivity of 10^{-3} in the intensity spectrum, to meet the sensitivity requirement of 0.1% (see sections 2 and 2.8). We wish to perform one fit per 20 nm wavelength interval, so each of these wavelength bins must contain enough spectral measurements to reliably fit a sinusoid to. According to the Nyquist sampling theorem, any signal which is band-limited to a frequency B can be fully reconstructed when it is uniformly sampled by samples which

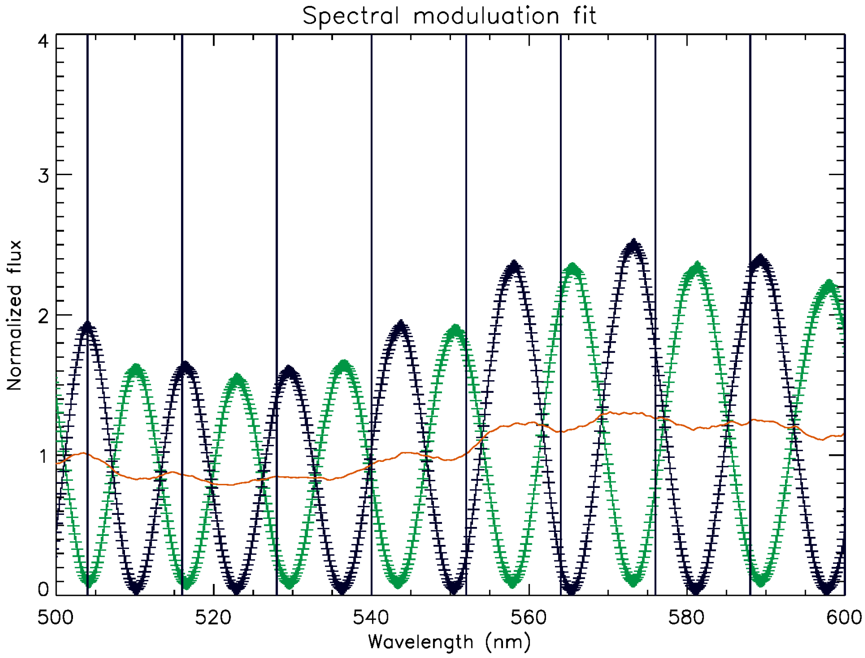

Figure 3.2: Measurement of a polarized source. The two orthogonal sinusoids stem from the two orientations of the linear polarizer. Averaging these gives the original spectrum s_0 (orange line). The wavelength regime is subdivided into bins of 20 nm, in each of which a pair sinusoids is to be fitted to the data.

are $\frac{1}{2B}$ apart. In this case, we are dealing with a spectral modulation with a period which we design to be 20 nm. This means that samples should be spaced 10 nm apart to obtain perfect sampling theoretically. This makes sense from a fitting-perspective: The period of the modulation is known (because it is determined only by the retardance of the MOR), so the amplitude and the phase of the modulation are the only two fitting parameters. Therefore in theory, two samples per bin should suffice. However, because the data contains noise, we require that the modulation be oversampled by a factor of ~ 3 to make sure that the amplitude of the modulation is correctly estimated with an accuracy of $\sim 10^{-3}$. This translates to a pixel scale of 3 nm px^{-1} or equivalently, an average spectral resolution of 200, and also conveniently fulfills the need of resolving the O_2A band, which has a width of 7.5 nm (see section 2.5).

Although the entire O_2A band only spans 7.5 nm while the spectrum is sampled at bins of 20 nm, a measurement of P_L and ϕ_L can nonetheless be performed within this band. Classically, polarization is measured differentially by subtracting measurements the of both polarization channels (see the discussion above). This differential measurement can also be applied directly to the modulated spectra generated by the SPEX setup: Subtracting the intensities of both channels at the location of the O_2A band constitutes a polarization measurement. However, this measurement will only depend on a small number of photons since only two or three spectral points are involved. Also, the efficiency is determined by the contrast between the two channels. If the O_2A band happens to be located at a wavelength where the two modulations cross, no polarization measurement can be performed. However, the phase ϕ_L of the modulation only depends on the orientation of the instrument with respect to the scattering geometry, which is a known parameter, since the instrument is fixed on the moon. Therefore, the retardance δ of the MOR can be made such that the modulation profile features maximum contrast at the location of the O_2A band. This application of the SPEX principle will be described in more detail by Van Harten (2013; to be submitted).

It should finally be noted that the frequency of the modulation is not constant with wavelength, but scales with $\frac{1}{\lambda}$. This means that if the data were to be oversampled by a factor of 3 at 600 nm, it would be oversampled by a factor of 2 at 400 nm and 4.5 at 800 nm, which are the edges if the wavelength regime. In order to sample reasonably well in the blue part of the spectrum, the data willthus be more intensely oversampled over the rest of the wavelength range. This is good for data reduction purposes but wasteful in terms of detector resources.

3.2 LOUPE-1A

Figure 3.3 shows a demonstration setup for SPEX. A broadband deuterium-halogen lightsource[1] feeds light into the the polarization optics through a 400 μm optical fiber[2]. The light is collimated by a fiber collimator[3] and sent through a quarter wave plate which is oriented along the vertical and a multi-order retarded rotated at an angle of 45° with the QWP (see section 3.1). The multi-order retarder is a combination of a MgF_2 crystal and an Al_2O_3 (sapphire) crystal, with a thickness ratio such that their mutual dependence of retardance on temperature cancel eachother. An a-thermal response is crucial for applications in environments where the thermal behavior is not constant, such as the lunar surface. The design of this combination of crystals is described in detail by Snik et al. (2009). Located behind the retarders is a polarizing beamsplitter which transmits the vertical linear polarization component and deflects the orthogonal component sideways. The beamsplitter acts as a polarization analyzer for both polarization directions simultaneously. Each polarization channel is subsequently fed into a fiber and carried to a dual channel spectrograph[4].

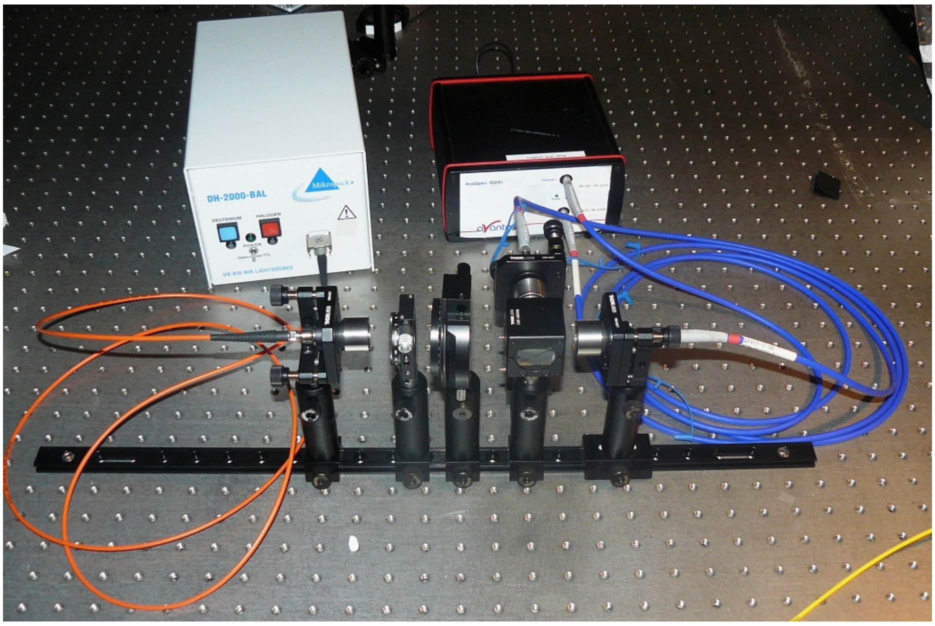

Figure 3.3: Photograph of the first implementation of the SPEX setup. Light is fed into the system through the optical fiber and the collimator lens on the left side of the image, then passes throuhg a quarter wave plate, multi-order retarder before the two linear polarization channels are split and sent off into two separate channels of the spectrograph.

---

[1] DH-2000-BAL He-D lamp

[2] Ocean Optics QP400-2-SR EOS-66777-7

[3] Thorlabs F810SMA-635

[4] AvaSpec-ULS3648-2-USB2

The output of the spectrograph with a polarized and unpolarized input is shown in figure 3.4 in which the modulation due to the fact that the source is significantly polarized, can clearly be seen. This serves as a demonstration of the SPEX principle in practice. For the purpose of LOUPE, the input should be adapted to accommodate for a larger field of view rather than to rely on a fiber-input. To create a field of view with a radius of 10°, we choose a 1.0" singlet plano-convex lens with a focal length of 35.2 mm[5] and an aperture in its front focal plane (see figures 3.5 and 3.6 for a schematic and a photograph). The clear aperture of this lens should be 17.6 mm (0.69") to encompass a rectangular half-field of view of 20° by 20° (see next section). We choose a circular entrance aperture with a diameter of 0.5 mm. The field at infinity will later be sliced into 50 × 50 points of which each 0.5 mm pencil beam has an instantaneous $f\#$ of 70, after leaving the objective lens.

It is important however, that the polarization optics is located as close to the front-end of the instrument as possible. Any optical components preceding the polarization optics cause systematics in the polarization measurements. The lens material is chosen to be fused silica because it has a low stress birefringence. This minimizes artificially induced polarizations by tensions in the lens. Also, because the lens is cylindrically symmetric, any polarization aberrations tend to cancel out if the field is point symmetrical. We therefore neglect spurious polarization signals induced by this lens for now.

3.2.1 Aperture and light gathering power

Astronomers often study sources which are very faint. This drives the development of large telescopes which capture as much flux as possible. In the case of LOUPE however, light gathering power is not expected to impose serious limits on the sensitivity of the instrument. What follows is a coarse estimate to prove this.

Figure 3.7 shows the amount of flux which the instrument is expected to register when placed on the lunar surface. In this simulation the Earth is irradiated by a solar flux of 1360.8 Wm^{-2} (Kopp and Lean, 2011), which is spectrally distributed as if the Sun were a blackbody of 5777 K (Pavlenko et al., 2012). Multiplying with the bond albedo of the Earth yields an estimate of the amount of flux which the Earth reflects back into space (spectral radiant exitance). The bond albedo is taken to be equal to 29.0% (Kim and Ramanathan, 2012) and is assumed to be spectrally gray. The spectral radiant exitance of the Earth is multiplied by the projected surface area of the Earth which is visible (depending on the phase angle: $A = \frac{\alpha}{180^\circ} R_\mathrm{e}^2$) and subsequently multiplied with the square of the ratio of the lunar orbital distance (3.8×10^5 km on average) over the Earth's radius (6.4×10^3 km) to yield the total amount of Earthshine flux which reaches the Moon (irradiance). This is multiplied by an assumed optical transmission of 10% and a quantum efficiency of 40% to yield an estimate of the amount of flux reaching LOUPE's photodetector. Finally, this is multiplied with the photon energy at each wavelength, to yield the number of photons which are registered by LOUPE per second at each wavelength, per square millimeter of aperture.

In order to measure a polarization signal of 0.1% $\left(10^{-3}\right)$ in a certain wavelength interval, the instrument needs to measure 10^6 photo-electrons in that wavelength interval. This is because shot noise scales with the square root of the integrated amount of photo-electrons (Sparks et al., 2012). The instrument will take one polarimetric measurement per 20 nm of wavelength, so 5×10^4 photo-electrons nm^{-1} are required. As can be seen from figure 3.7, the count rate is high enough to exceed 5×10^4 in less than a second of integration, even for apertures smaller than 1 mm^2. Therefore we will assume the aperture to be small compared to the focal length of the objective lens and that exposures can be treated as if

---

[5] Thorlabs LA4052-A

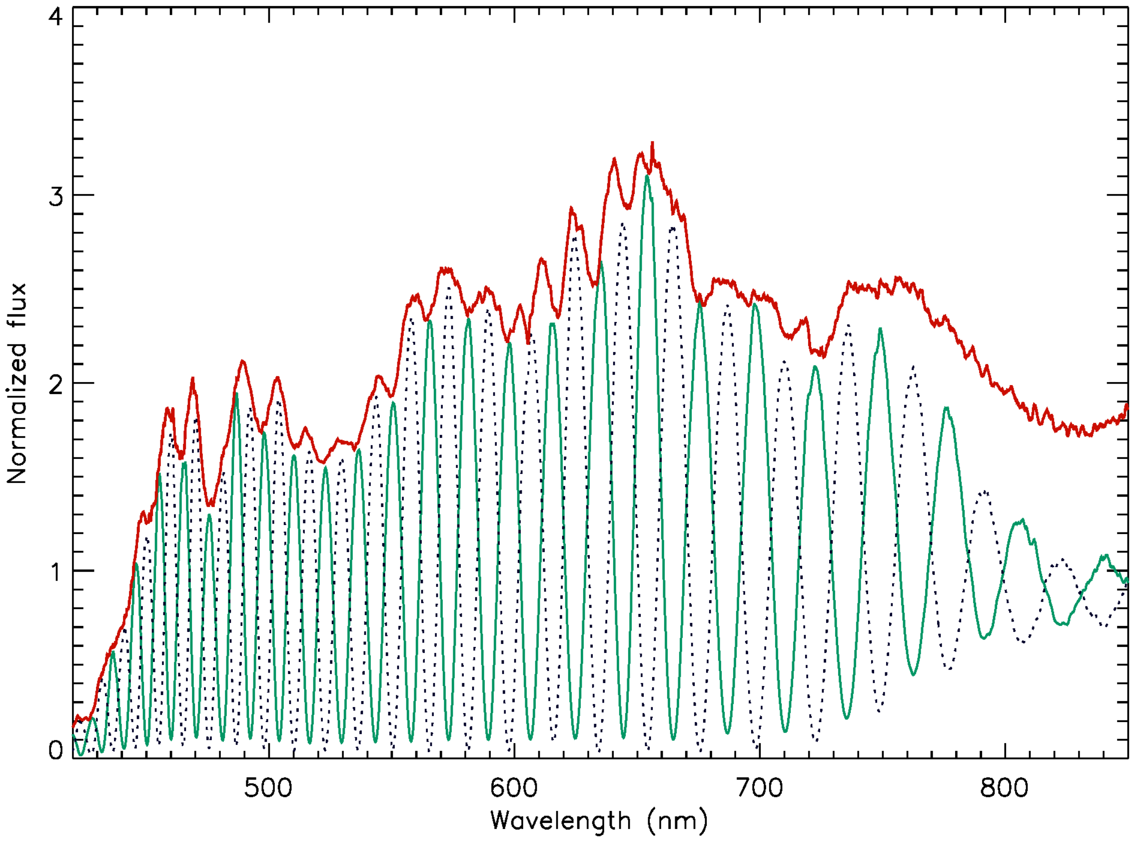

Figure 3.4: Reponse of the system shown in figure 3.3 to an input which was polarized using a linear sheet polarizer. The plot shows both polarization channels (solid green and dashed lines) and their sum (red line) which is equal to the original spectrum in the case of ideal optics. In this implementation, some imperfections can be discerned. Most notably, the amplitude of the polarization modulation diminishes beyond 700 nm. This can likely be attributed to a breakdown of the linear polarizer used to polarize the source, which does not effectively polarize at longer wavelengths (also see section 5.5). Also, the overarching spectrum clearly features a residual modulation pattern, which is likely caused by spectral misalignment of the two channels.

they were instantaneous.

Wavelength calibration

The spectrograph features 3648 pixels at wavelengths roughly between 360 nm and 910 nm. The pixel grid is calibrated in wavelength using a mercury-argon linelamp[6]. We use 22 lines to fit a 4^{th} order polynomial to the known line positions. This gives the wavelength solutions of both of the spectrograph's channels, which is shown in figure 3.8.

Test observations

To test the response of this setup to an extended physical object with partial polarization, we place a styrophome sphere 2 m in front of the aperture of the instrument shown in figure 3.6. The sphere has a diameter of 7 cm so it has an angular diameter of 2° as seen from the instrument which matches the angular size of the Earth as seen from the Moon. The sphere is illuminated by a projector lamp from different angles (see figure 3.9). Figure 3.10 shows field integrated measurements of both polarization channels of light reflected by

---

[6] Ocean Optics HG-1 Mercury Argon calibration source

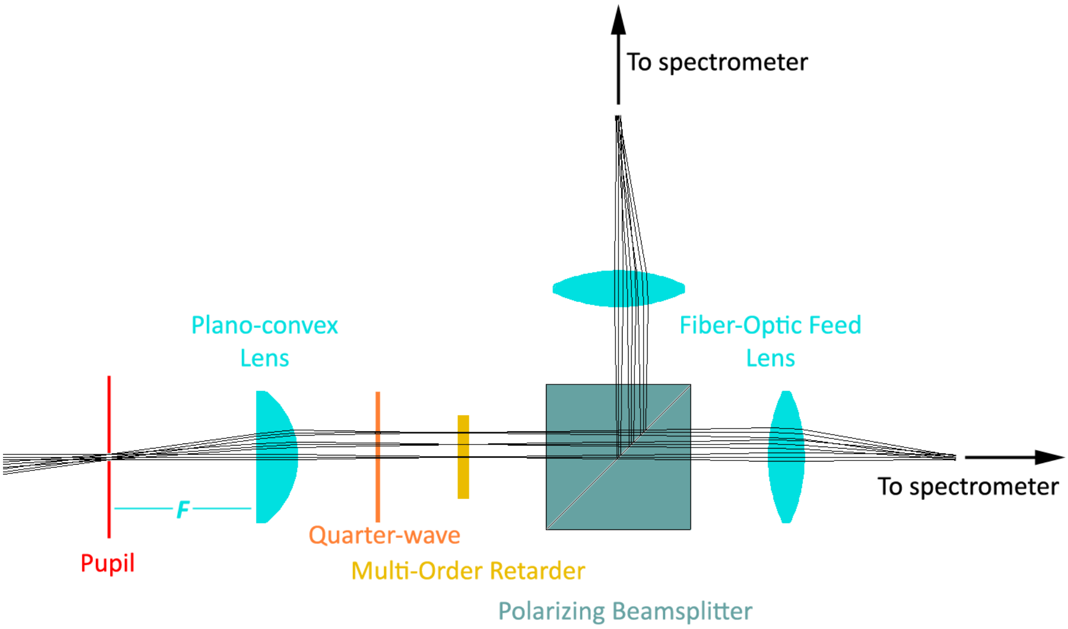

Figure 3.5: Schematic of the implementation of LOUPE-1A. The fiber input of the SPEX setup described in section 3.1 has been replaced by a plano-convex lens with an aperture in its focus. Depending on the focal length and size of the lens, this generates a field of view which is large enough to capture the entire libration curve of the Earth. Because the aperture is in the focal plane of the lens, the beam exiting the lens is collimated, and can thus pass through the rest of the system in the same way as fiber-fed setup shown in figure 3.3

.

the styrophome target for illumination angles of 45° and 90°. In both measurements, the spectral modulation which is indicative of linear polarization is clearly visible by eye. We can therefore conclude that performing disk-integrated spectropolarimetry can be implemented with relative simplicity. In the next section, the addition of spatial filtering will be discussed.

3.3 LOUPE-2A

Spatial resolution

The design for LOUPE-1A shown in figure 3.5 gathers all of the incoming light, imprints the spectral modulation due to the average polarization state of all light in the field and then sends both polarization channels to a spectrograph by means of a pair of optical fibers. In order expand this design to maintain spatial resolution, certain parts of the collimated beam (figure 3.5) which leaves the primary lens (i.e. certain parts of the field) should be analyzed separately.

An effective way to spatially filter the beam is by using a two-dimensional *microshutter array*. By sequentially opening and closing the microshutters, the spectropolarimetric measurement can be performed for each field position separately and the entire field is scanned. Depending on the dimensions of the microshutters and the total size of the array, the microshutter array could simply be inserted in the setup of LOUPE-1A (figure 3.3), at nearly any position in front of the polarizing beamsplitter. When the microshutter array would be opened completely, the instrument would be equivalent to LOUPE-1A and it could take a

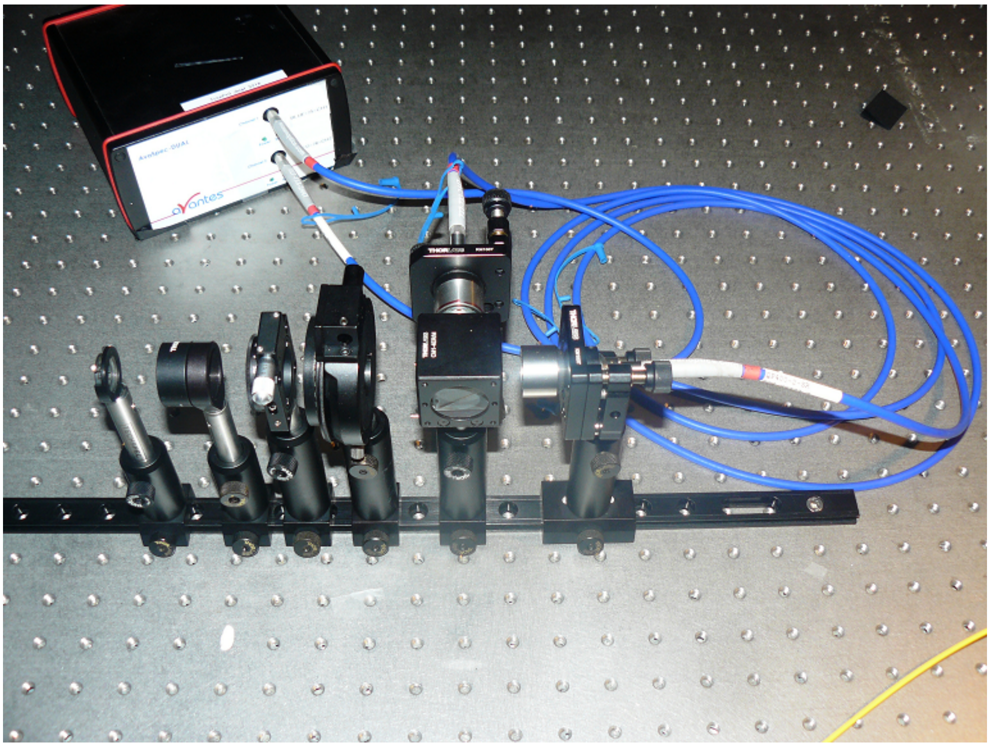

Figure 3.6: Photograph of the setup for LOUPE-1A of which the schematic is shown in figure 3.5. Light enters the system through the aperture on the far left and is subsequently collimated by the objective lens after which it passes through the polarization optics which are the same as in figure 3.3

.

purely unresolved measurement; whereas when only a single microshutter would be opened, only that part of the field would be fed into the spectrometer and the same measurement could be performed albeit with a longer integration time. The apparent simplicity associated with a microshutter array is offset by the fact that this is a new piece of technology which is only finding its first space application in the NIRspec instrument aboard the James Webb Space Telescope (Mott et al., 2001). The device relies on the mechanical movement of the microshutters (prone to failure) and consumes electrical power for operation. Although theoretically, the microshutter array seems to be perfectly suited for the application of LOUPE-2A, these traits lead us to discard it in favour of a proven, more robust solid state solution.

We employ a *Microlens array* (MLA) which is a two-dimensional array of lenses rather than shutters (see figure 3.11). The MLA is placed in the back-focal plane of the objective lens so that the aperture is re-imaged by each of the microlenses with a magnification which is equal to the ratio of the focal distance of the MLA f_2 and that of the objective lens f_1. The magnification is constant across the field because this is a double-telecentric configuration. f_2 is generally small compared to f_1, so each microlens will produce a micro-image of the pupil, each from a different line of sight. Between the primary lens and the MLA, the beam is nearly collimated, so this is where we insert the polarization optics. The polarizing beamsplitter is replaced by a wire-grid (linear) polarizer, so the dual channel capability is lost. This is an issue which will be discussed later.

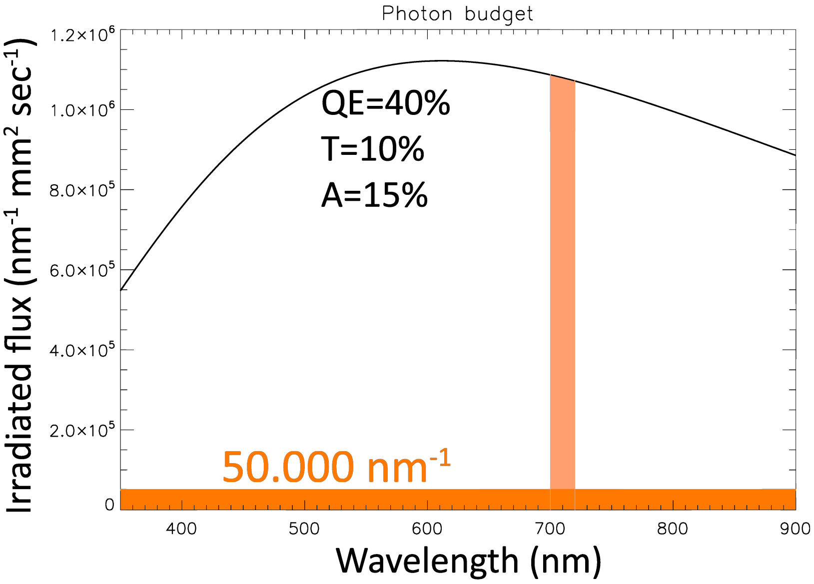

Figure 3.7: Estimated irradiance due to Earthshine onto the instrument, when located on the lunar surface. The incoming flux is modeled as a black-body spectrum corresponding to 5777 K, which was reflected by Earth and propagated to the lunar surface. The y-axis denotes the number of photons which reach the lunar surface per nm wavelength per second per square millimeter of aperture. The pink highlighted area marks a wavelength bin of 20 nm in width, which is the presumed spectropolarimetric resolution of the instrument. In order to achieve a 10^{-3} sensitivity, this bin must contain at least 10^6 photons, which it clearly does. The orange area denotes the equivalent photon flux which is needed to satisfy the sensitivity requirement, which is 50000 nm^{-1}. Across the entire wavelength range, this requirement is easily satisfied.

Imaging spectropolarimetry

The microlens array generates an array of micropupil images. Each of these contain the light coming from a different area within the field and contain the spectral encoding of the polarization information. Each micropupil must thus be spectrally dispersed and re-imaged separately to reveal the spectropolarimetric modulation of each field point. Re-imaging of the image plane of the MLA is to be performed by a double-telecentric pair of lenses which must have a near-perfect imaging performance across a large range of wavelengths (400 nm – 800 nm) and field angles (±10°). Figure 3.12 shows a raytracing simulation, in which the re-imaging lenses are modeled as ideal lenses. Between these re-imaging lenses, the beam is collimated. Here we insert a dispersion optic like a prism or a transmission grating, which will spectrally disperse the micropupils an unravel the spectral imprint due to any polarization, see figure 3.13.

In order to achieve a high efficiency in detector usage, the MLA is rotated with respect to the dispersion optic. The grid formed by the micropupils is thus rotated with respect to the dispersion direction, so that spectra can be stacked more efficiently onto the detector (see figure 3.14). The stacking efficiency depends on the dimensions of the spectra: The longer the spectra are (the higher the spectral resolution is), the closer they have to be stacked together to prevent overlapping at the edges of the wavelength regime. Conversely, the lateral distance between spectra is limited by their maximum width, i.e. the largest spot size in the wavelength regime. Therefore, the spectral resolution is directly limited by the performance of the re-imaging lenses. In turn, the achievable spectral resolution

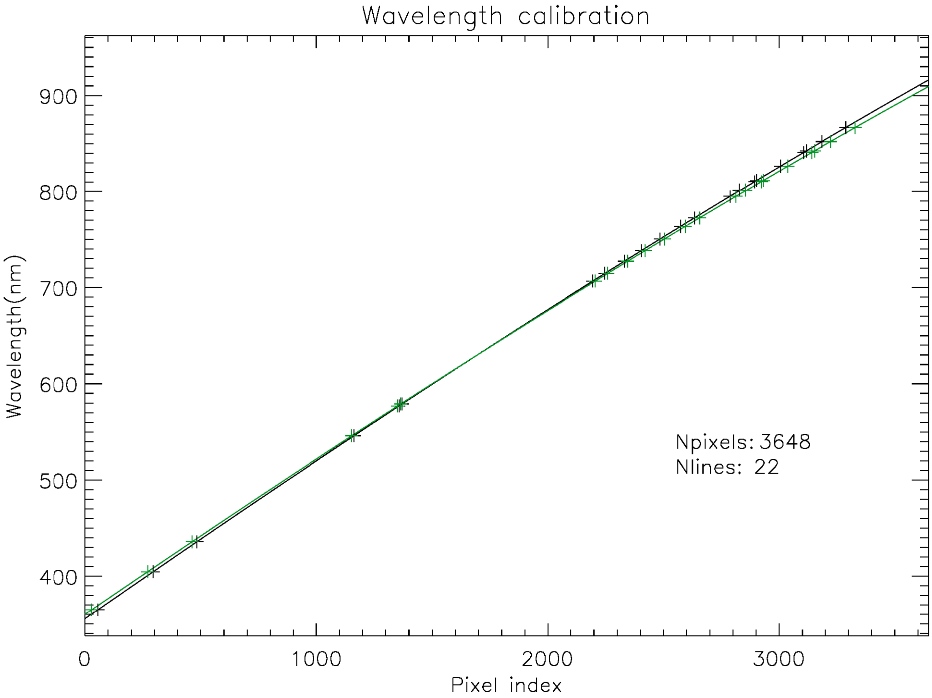

Figure 3.8: The wavelength solution as determined using a mercury-argon line lamp, for both spectral channels of the spectrometer.

Figure 3.9: Styrosphere target used to model the sunlight scattering off of Earth. The target is illuminated by a movable broadband projector lamp.

determines the required pixel scale, i.e. at which spatial resolution the grid of microspectra can be sampled. Here we must take the total size of the field into account: A fine pixel grid will require a large detector array to fill the entire field. Antichi et al. (2009) formulated an optical scheme which can be used to maximize the performance of integral field spectrographs, while minimizing the required number of detector pixels. The required spectral resolution is 3 nm px^{-1}, so the total amount of pixels needed per microspectrum is at least 133. The entire field being sampled by 50×50 spatial samples, at least 3.3×10^5 pixels are

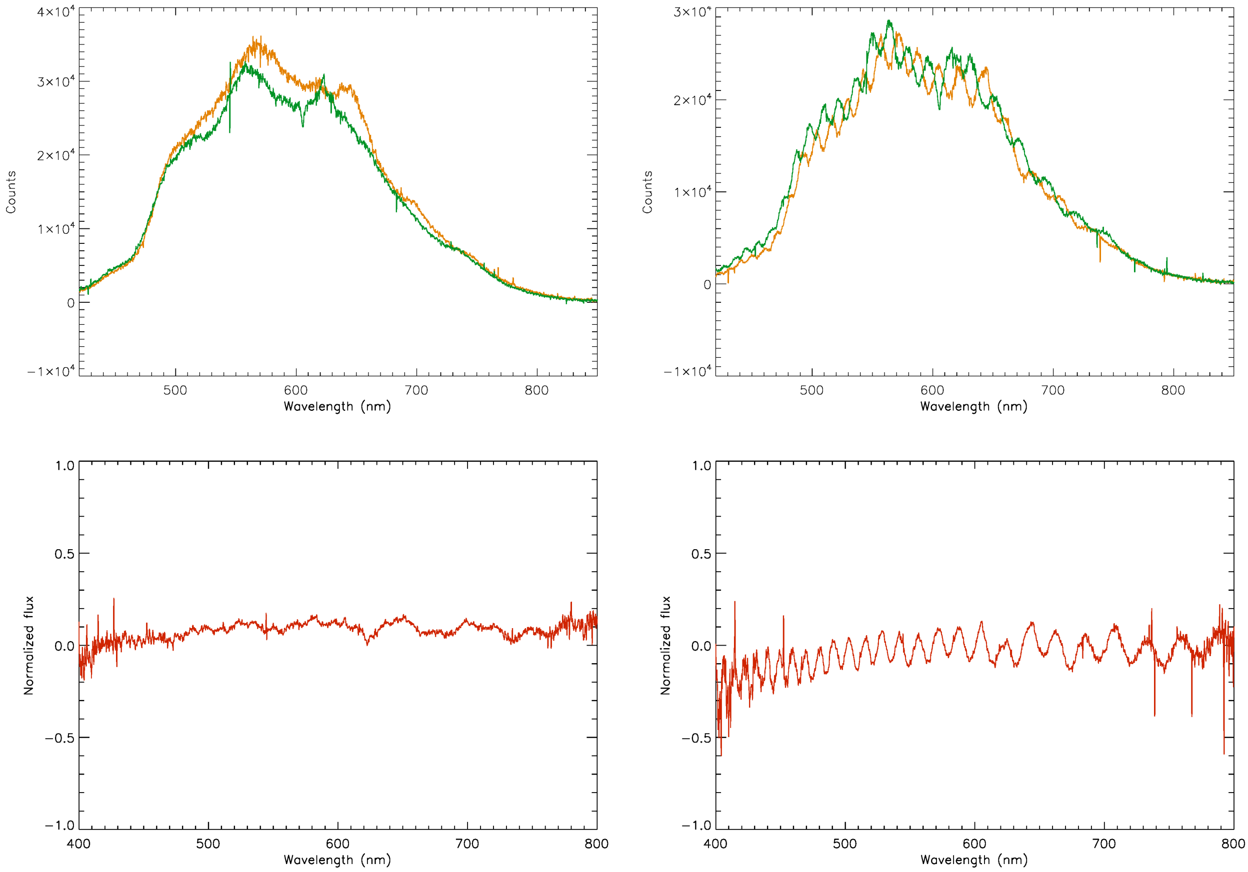

Figure 3.10: The top panels show the field-integrated spectral energy distribution of the styrophome target, for both polarization channels, after subtraction of the dark-current and a background measurement. The styrophome target was illuminated at phase angles of $\sim 25°$ (left) and $\sim 80°$ (right) and spectra are shown for both polarization channels. The panels below show the corresponding visibility of the modulation pattern due to the presence of a polarized component: $\frac{I1-I2}{I1+I2}$. It is clear that towards 90° phase-angles, the signal is more strongly polarized.

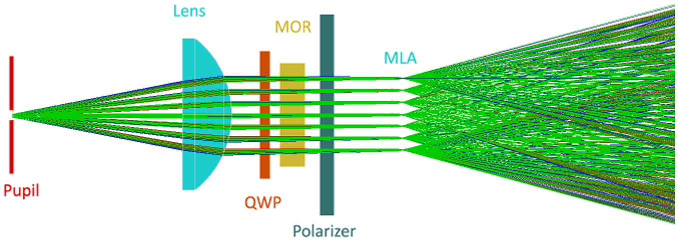

Figure 3.11: To preserve spatial information, different parts of the field must be analyzed separately. In this design, spatial separation is accomplished by inserting a micro-lens array at the back-focal plane of the primary lens, after the spectropolarimetric modulation imprint has been performed. The aperture is thus re-imaged by each microlens. These *micropupils* each see a different part of the field, and are analyzed separately.

needed to sample the entire field in the case of optimal spectral sampling and arrangement on the detector. Although detector economy is of little concern for the design of this prototype, it must be noted that astronomical space instruments with detectors which are larger than 2MP are rare, so advanced optimization of the arrangement of the microspectra on the detector will likely be crucial in following iterations of development.

Including the fore-optics, the length of the instrument measures $2f_1 + f_2 + 4f_3 \approx 2f_1 + 4f_3$. The strongest contribution to the instrument size therefore comes from the re-imaging lenses, for which it is also most crucial that they have an aberration-free performance which generally means that they should be slow. Here we thus note a direct balance between instrument size and optical performance (hence spectral performance) in this design. Therefore we need to explore experimentally what re-imaging performance can be achieved before the theoretical design can be continued. This thus concludes the design concept of LOUPE-2A.

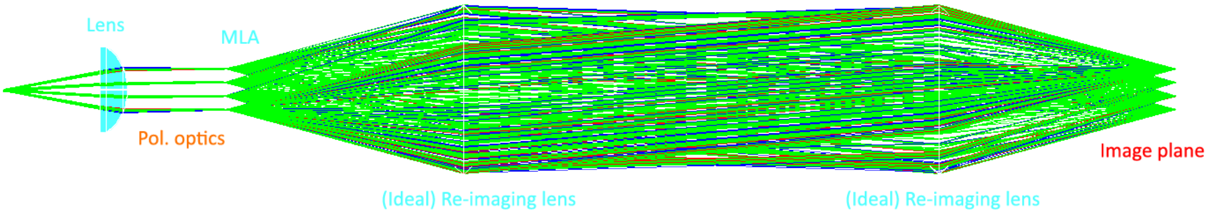

Figure 3.12: Raytracing simulation of the objective lens, MLA and re-imaging optics. The two re-imaging lenses are modeled as ideal lenses, and provide one-to-one re-imaging of the grid of micropupils in the MLA image plane, onto the detector which is not shown.

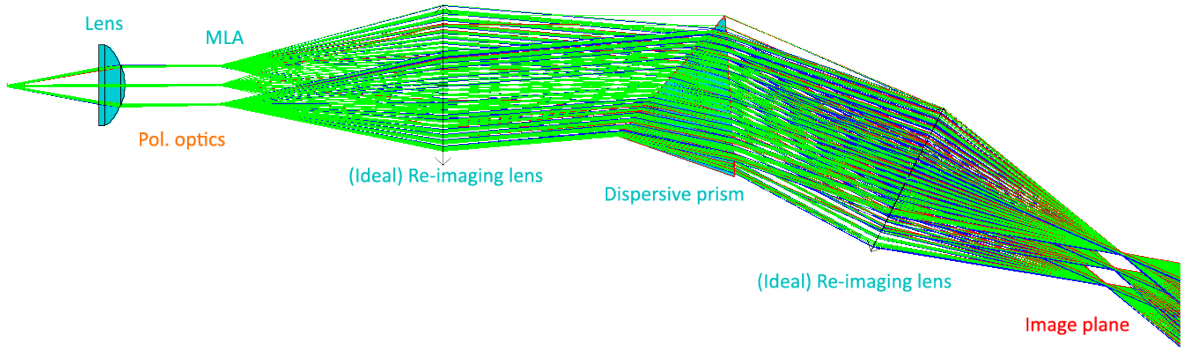

Figure 3.13: In order to spectrally disperse the re-imaged grid of micropupils, a dispersive optic such as a prism is inserted between the re-imaging lenses. Modeled here is a fused silica prism with a 45° top angle, rotated by 19° to approximately equalize the incidence angle and the angle of the refracted ray.

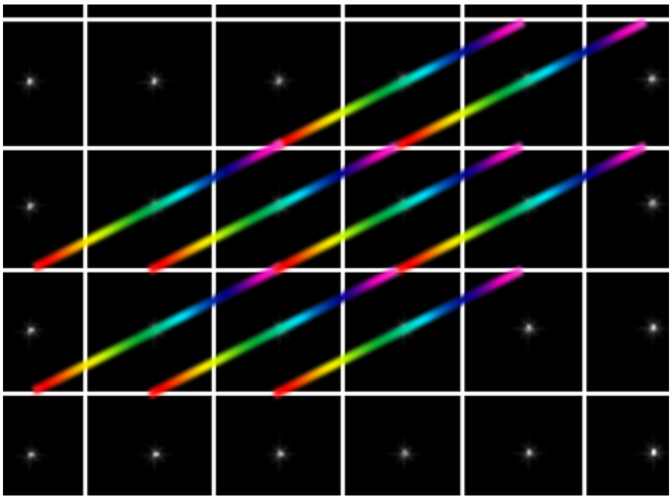

Figure 3.14: The grid of micropupils (here sliced in square regions for illustration purposes) is rotated with respect to the dispersion direction, to allow for efficient use of detector resources. Spectra should be stacked end-to end without overlapping.

Chapter 4

Prototype implementation

This chapter deals with the implementation of a prototype for LOUPE-2A. The purpose of the prototype is not to match the requirements which flow from the science case, but to map out the practical difficulties and limitations which must be overcome before a flight-model can be constructed. The prototype will indicate the amount of effort which will be needed to meet the science case in following iterations. The design concept is shown in figure 3.13 and the following sections will treat our choices for the different components in detail.

4.1 Objective lens

In order to demonstrate the scientific merit of LOUPEs prototype, we aim to perform observations of the polarization spectrum of the Moon. Observing the Moon from Earth is analogous to observing the Earth from the Moon, but the angular size of the target needs to be scaled down by a factor of 4 because the Moon measures 0.5° on the sky whereas the Earth measures 2° as seen from the Moon. This is easily done by replacing the objective lens ($f_1 = 35.2$ mm) by a lens which has a focal length which is approximately four times larger ($f_1' = 150$ mm), and increasing the aperture diameter to 2 mm. By doing this, the entire field is demagnified by a factor of 4, but the size and spacing of the spots (and thus the sampling of the microspectra and the irradiance) have remained constant. The analysis which follows will be based on observations taken with the $f_1 = 150$ mm lens, but the setup is completely analogous to the Earth-observing case in which the $f_1 = 35.2$ mm lens would be used.

4.2 Microlens array

The Microlens array is a rectangular 15.0×15.0 mm^2 grid of square microlenses measuring 222 μm each, with a focal distance of 0.93 mm [1], see figure 4.1. The circular extent of the collimated beam is 17.6 mm. By dividing by $\sqrt{2}$, we switch to a rectangular field of $20° \times 20°$, which limits the beam size to 12.4×12.4 mm^2. The rectangular field is therefore sampled by 56×56 microlenses (which exceeds the required 50×50 samples). Although we do not physically mask the beam in a rectangular fashion, these beam dimensions are used from now on to simplify the discussion concerning the rectangular nature of the micropupil grid and the rectangular geometry of the detector.

Each microlens creates a demagnified image of the the pupil in the focal plane of the MLA, with a magnification factor of $\frac{f_2}{f_1} = 2.6 \times 10^{-2}$. The diameter of each micropupil image is therefore 13 μm. This is comparable to the size of a detector pixel (detector pixel scales range between $\sim 2 - 20$ μm). For each microlens, any optical aberrations will thus be assumed to be small compared to the pixel scale of the detector. On the same token,

---

[1] APO-Q-P222-F0,93, http://www.okotech.com/microlens-arrays

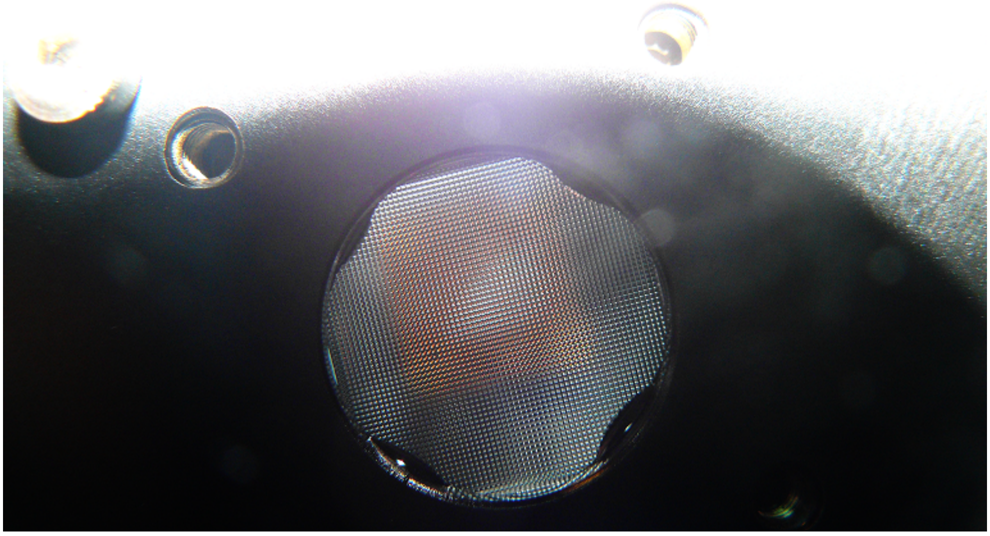

Figure 4.1: Photograph of the MLA, mounted in a rotation mount. The MLA measures $15 \times 15\text{mm}^2$. The microlenses are spaced 222 µm apart with a fill-factor of 99%.

because the the incoming pencil beams converge slowly ($f\# = 70$) compared to the size of the microlenses, axial aberrations of the focal plane of the first lens have very little impact on the quality of the micropupil images. Only if the spot size of the objective lens would be larger than the extent of the microlenses, the spatial resolution would be limited by the objective lens. Otherwise, the image quality of the entire system is expected to be dominated by the re-imaging lenses.

4.3 Polarization Optics

The polarization optics are placed in the collimated part of the beam, between the objective lens and the MLA. As described in section 3.1, it consists of a quarter-wave plate, a multi-order retarder and a linear polarizer. To accomodate the larger beam size, these components are not the same as those in the implementation of LOUPE-1A (section 3.2)[2],[3]. Most notably, the a-thermal multi-order retarder was replaced by a stack of 9 $3.9\lambda - 4.0\lambda$ retarding films, to produce a total retardance of approximately 39.5λ at 560 nm (see figure 4.2 for a photograph of this part of the setup). Although this implementation is not a-thermal, the technology related to a-thermalization of the MOR has already been proven and discussed, and the choice for this stack of 4λ films was purely a practical one.

4.4 Re-imaging optics

The MLA produces a grid of micropupils which are to be re-imaged onto a detector plane. Because of the short focal distance of the MLA, the light-cones coming from the microlenses have an angle of 13.5° (see figure 3.11). To capture all this light, the $f\#$ of the re-imaging lenses has to be small. This, together with the extent of the wavelength range rule out the use of simple spherical singlet lenses or achromatic doublets. Instead, we choose to use a pair of 2” photographic objective lenses[4] with a focal length of 85 mm ($f - \# = 1.7$, see image 4.3). In photography, high quality imaging properties across wide ranges of field angles and wavelengths are imperative. Although lens systems like these are obviously not

---

[2] Thorlabs WPQ10E-633

[3] Thorlabs LPVISE200-A

[4] Canon Ultrasonic EF85mm f/1.8 USM

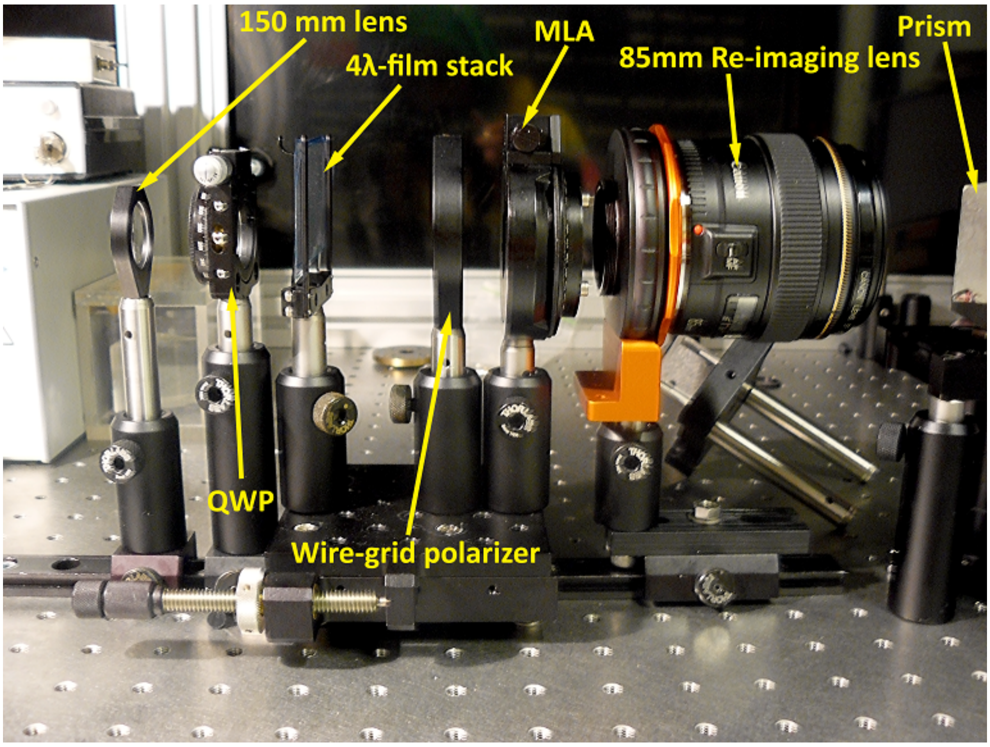

Figure 4.2: Photograph of the front-end of the setup of LOUPE-2A. The MLA is placed on a movable platform which is used to position it precisely in the focal plane of the re-imaging lens. See section 4.4 Light enters from the left side of the image through an aperture which is located beyond the left border of the photograph.

space-qualified, they are well suited for the purpose of this prototype. At 85 mm behind the focal plane of the MLA, the beam measures 32.5×32.5 mm^2, so the circular clear aperture of the re-imaging lens pair should be at least 37.7 mm or 1.48". These objective lenses are therefore large enough, and do not cut off parts of the beam, nor do we approach the edge of their field, where the performance might be degraded.

4.5 Camera

As the photographic objective lenses re-image the micropupil grid without any magnification, each micropupil image (and thus each spectral point) will measure at least 13 µm [5]. To avoid undersampling, we require a detector which has a pixel size at least twice as small. We choose a 1.2 MP Point-Grey Flea3[6] CMOS camera with square pixels of 5.3 µm (figure 4.4 shows the quantum efficiency of the chip). The detector array measures 6.8×5.4 mm^2. For practical purposes however, this camera was favored over larger detectors, even though only a quarter of the field is covered. CMOS technology has the advantage that certain parts of the array can be read selectively. This is an important advantage of the use of this type of detectors in space, where data bandwidth is limited. In the case of LOUPE, only the part of the detector on which the Earth is imaged, needs to be read out. Including considerable margin, the Earth might cover only some 100 field points at any given instance. This means that only about 4% of the chip needs to be read, as the field measures 50×50 field points.

---

[5] The re-imaging lenses were modeled to be aberration-free, so the 13 µm spot size is a lower limit. Therefore, with this choice of sampling, we expect to oversample the data. Also see section 4.6.

[6] Point Grey FL3-U3-13E4M-C

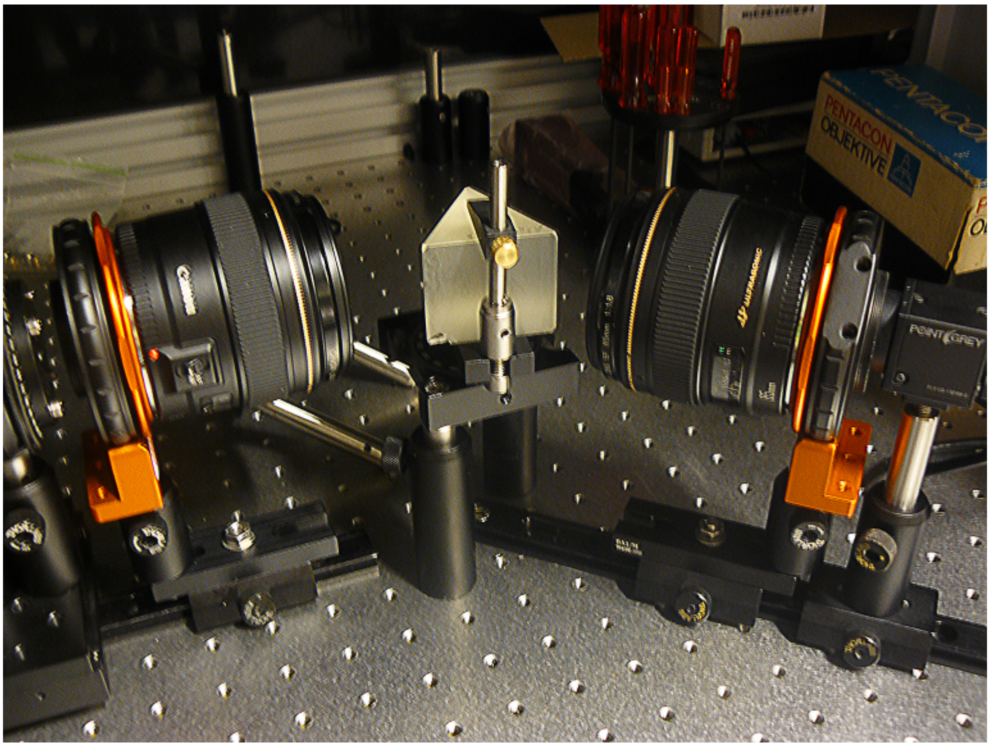

Figure 4.3: Re-imging optics. The MLA is located on the far left of the picture, in the focal plane of the first re-imaging lens. The second re-imaging lens is aligned off-axis, because the dispersive prism between the two lenses refracts the beam, see section 3.3 and figure 3.13. The camera is located on the far right of the image, see section 4.5.

The A/D converter has a depth of 10 bits (1024 steps in intensity). This means that when the full dynamic range of the camera can be used, the sensitivity of the detector is 10^{-3}, which matches the sensitivity requirement (section 2.2). In reality however, the dynamic range will not be fully usable everywhere in the field, so the sensitivity of the prototype will likely be limited by the camera's pixel depth. This is an issue with this specific choice of camera and is not a fundamental limitation to the space application of LOUPE.

4.6 Dispersion

Each spectral spot being assumed to be close to 13 µm in size, we can now determine which dispersion is approximately needed to produce microspectra which are well-sampled across the entire wavelength range. In the middle of the wavelength range, we require a resolution of ~ 3 nm per spectral pixel (see section 2.2), so each microspectrum will be at least ~ 1.7 mm or 320 detector pixels in length. The grating equation for a transmission grating at normal incidence gives us the diffraction angle as a function of wavelength, and thus the dispersion $d\theta$:

$$\sin(\theta) = \frac{md}{\lambda}$$

$$d\theta = \|\theta_{\max} - \theta_{\min}\| = \arcsin\left(\frac{md}{\lambda_{\min}}\right) - \arcsin\left(\frac{md}{\lambda_{\max}}\right)$$

Here d is the grating constant and m the diffraction order, which we assume to be equal to unity. The dispersion angle and the length of the microspectra on the image plane are related by the back-focal length of the last re-imaging lens:

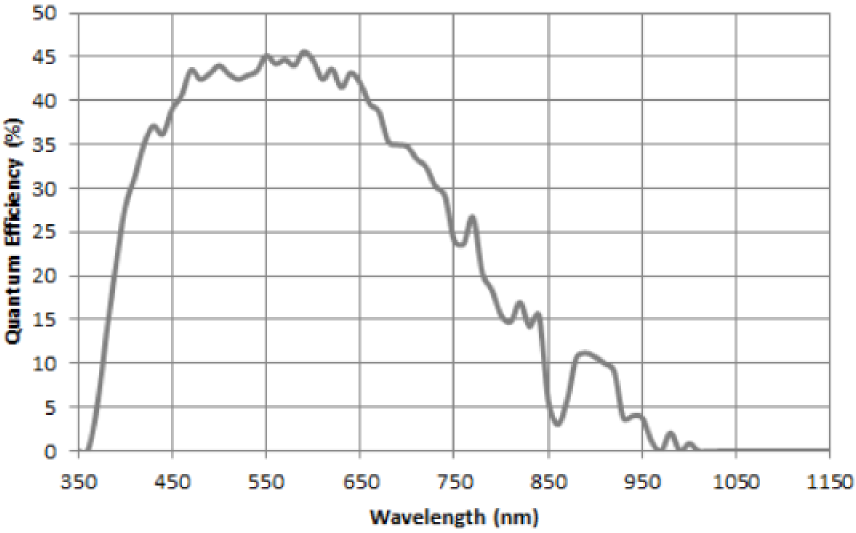

Figure 4.4: Quantum efficiency of the camera plotted against wavelength. Figure adopted from the Point Grey Flea3 technical reference manual.

$$L = f_4 \tan(d\theta)$$

We find that in order to achieve a length L of 1.7 mm, a dispersion of 1.2° is needed, which means that the grating constant should amount to 47 lines mm^{-1}. For practical reasons, such a grating could not be implemented.

Instead we turn our attention to dispersive prisms. The combination of different glass materials and prism geometries allows for a wide variety of dispersion properties. The prism with top angle A is inserted in the collimated beam between the re-imaging lenses, such that a ray impinges onto the first surface of the prism at an angle of incidence α. It is then refracted towards the normal of the first surface under influence of Snells law, at refraction angle θ:

$$sin(\alpha) = n(\lambda) sin(\theta)$$

The ray then meets the second surface of the prism (which is oriented at an angle $\beta = A - \alpha$ with respect to the optical axis) at an angle of incidence ϕ and is refracted away from the normal at an angle γ, as it leaves the prism. The angle ω under which the ray exits the prism is therefore: $\omega = \gamma - \beta = \gamma - A + \alpha$ (see figure 4.5. Solving for ω using the repeated application of Snells law, gives:

$$\omega(\lambda) = \arcsin\left(n(\lambda) \sin\left(A - \arcsin\left(\frac{1}{n(\lambda)} \sin(\alpha)\right)\right)\right) + \alpha - A \tag{4.1}$$

The dispersion angle therefore is:

$$d\omega = \|\omega_{\text{max}} - \omega_{\text{min}}\|$$

For different angles of incidence, the dispersion $d\omega$ for prisms made of these materials, was computed using equation 4.1 and the refractive indices for some common glasses shown in table 4.6. The results are shown in figure 4.6. It is evident that although the spectral dispersion can be fine-tuned by changing the angle of incidence (i.e. rotating the prism along an axis perpendicular to the beam), larger angles of incidence decrease the effective size of the aperture of the prism. For larger angles of incidence, larger prisms are thus required.

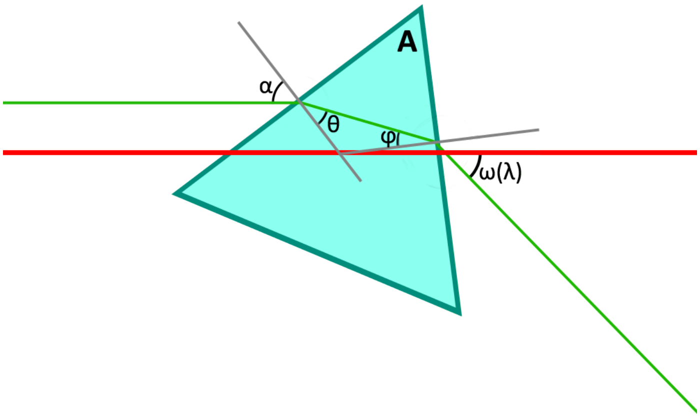

Figure 4.5: Schematic of the geometry of an equilateral prism. large angles of incidence α cause smaller dispersion angles, but also limit the effective aperture of the prism.

	400 nm	780 nm
BK7	1.53024	1.51106
UVFS	1.46962	1.45356
SF11	1.84208	1.76558
F2	1.65064	1.60889
CaF2	1.441	1.430

Table 4.1: Index of refraction for some common glasses at wavelengths of 400 and 780 nm, adopted from the Material handbook of CVI Laser Optics and Melles Griot. Note that the refraction indices for Calcium Floride are interpolates from neighbouring values at 355 and 486 nm, and 700 nm and 1 µm.

In the case of ideal imaging, each spectrum would be 13 µm in width, which would enable very efficient stacking (see section 3.3). In reality however, the re-imaging system will aberrate the micropupils and thus the spectra will be wider than 13 µm towards longer and shorter wavelengths. Provided that the aberrations are not severe, figure 4.6 gives a good indication of what type and size of prism is needed.

In the laboratory, a 25 mm BK7 prism, with a top angle of 45°[7] was readily available. The aperture of the prism being smaller than the size of the beam, means that a lot of vignetting occurs. In the current setup this is not a problem because the detector is also much smaller than the total extent of the field, so most of the field is lost regardless (see section 4.5). A larger prism of unknown composition, with a top angle of 54° was also available (shown in figure 4.3).

Because the true spot size of the re-imaging system is unknown at this point, we must resort to test measurements to determine what the imaging quality the objective lenses can achieve. This will determine the efficiency at which spectra can be stacked onto the detector

---

[7] Thorlabs PS911

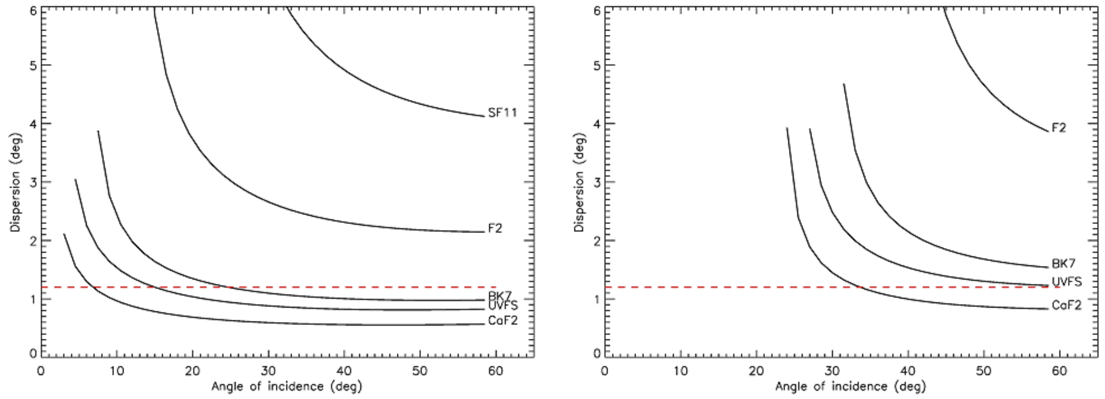

Figure 4.6: Dispersion as a function of angle of incidence for prisms made of different glasses with top angles of 45° (left) and 60° (right). The dashed red line indicates the amount of dispersion which is needed to generate microspectra with 1.7 mm in length. One of the prisms which we use is a 45°-top angle BK7 prism.

and thus how much spectral resolution or spectral bandwidth can actually be afforded in reality.

Chapter 5

Performance analysis

5.1 Imaging performance and field characteristics

To test the imaging performance of the system, we illuminate the entrance aperture with the halogen source also used to test LOUPE-1A (see section 3.2). The beam exiting the fiber is first collimated and then focused on to the 2.0 mm aperture by a pair of singlet lenses. The focal distance of the latter lens matches that of LOUPE's original objective lens (35.2 mm rather than the 150 mm lens which is implemented for these test observations), so although much of the beam is vignetted, the entire field is illuminated. This illumination is assumed to be roughly uniform (the uniformity is mostly limited by the uniformity of the fiber output) and no effort is taken to remove field variations in illumination intensity. We remove the dispersive prism (see figure 3.12 so that an image of the entire grid of micropupils is obtained, with the goal of evaluating the performance of the re-imaging lens pair. The resulting image is shown in figure 5.1. Although this image represents only a relatively small ($\sim 25\%$) part of the actual field, it is worthwhile to note that departures from field uniformity appear to be small.

In order to measure the performance of the re-imaging system, we wish to measure the average extent of the images of the spots generated by the MLA. We define the spot-size as the diameter of a circle centered on the spot, which contains 95% of the light. To this end, 7 randomly selected spots are subjected to a 2D Gaussian fit. The fitting routine returns a measure for the standard deviation of the Gaussian in both dimensions (σ_x and σ_y). The diameter of the circle containing 95% of the light is $4\sigma = 4\sqrt{\sigma_x^2 + \sigma_y^2}$, assuming a point-symmetric Gaussian profile and is measured to be 33.4 µm. One of the seven randomly selected spots is shown in figure 5.2.

5.2 Spectral configuration and performance

Taking the same illumination system as before, but inserting the dispersive prisms, the grid of spots shown in figure 5.1 is smeared out in the horizontal direction. Careful rotation of the MLA around the optical axis separates the horizontal smudges into separate spectra, while rotating the dispersive prism around the vertical adjusts the amount of dispersion and thus the length of the spectra (see figure 4.6). Results for both prisms are shown in figure 5.4. In both implementations, the wavelength range needed to be cut at the red and blue ends of the bandwidth because the spot size at the edges of the bandwidth due to aberrations, prevented effective stacking of the spectra. The wavelength range using the BK7 prism was limited to $450 - 750$ nm while the spectral range using the larger prism which has a higher dispersion, was limited to $600 - 750$ nm. The bands were cut using the

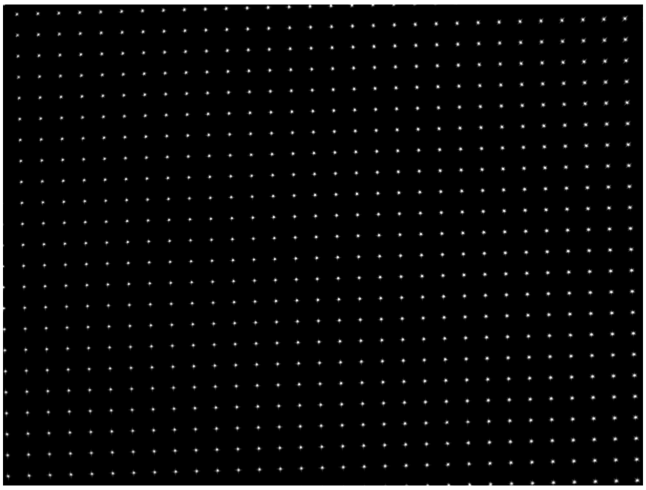

Figure 5.1: Grid of undispersed micropupils. Intensity variations and distortions across the field appear to small. The MLA is slightly rotated with respect to the camera, so the micropupil grid is not perfectly aligned with the chip.

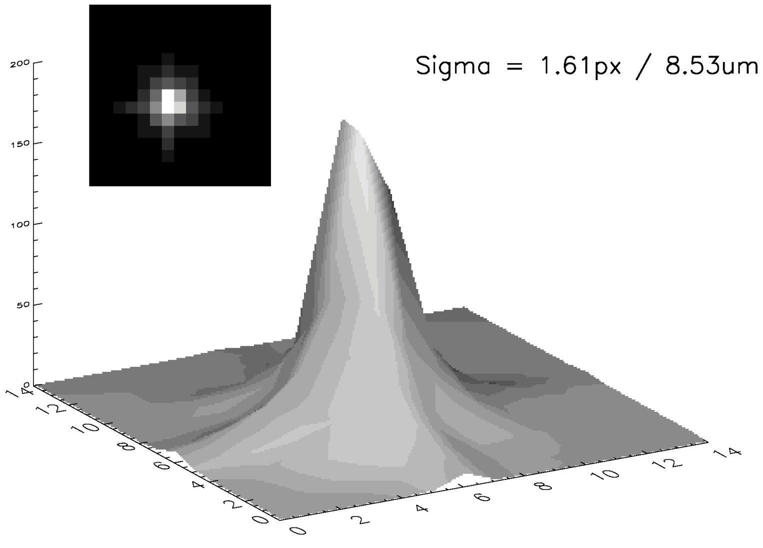

Figure 5.2: A micropupil as imaged by the re-imaging lens pair. This spot is one of 7 random spots in the field for which the spot's sizes ware calculated by fitting of 2D gaussian profiles. On average, the fitted standard deviation σ equals 1.58px, or 8.36 µm. This means that 95% of the light in each spot is expected to fall within a circle with a diameter of 33.4 µm. This spot-size is the limiting factor in the stacking-efficiency of the micro-spectra (see section 3.3).

combined use of long and short-pass edge filters[1][2][3], placed between the pair of collimator lenses in the illumination system (see figure 5.3).

The spectral resolution is primarily limited by the spot size of the re-imaging system, which is a function of wavelength. Near the edges of the band aberrations decrease the image quality, decreasing the spectral resolution at these wavelengths. For the implementation of the BK7 prism, the spot size increases to roughly 10 px (53 µm) at 750 nm. 53 µm cor-

---

[1] Thorlabs FEL450

[2] Thorlabs FEL600

[3] Thorlabs FES750

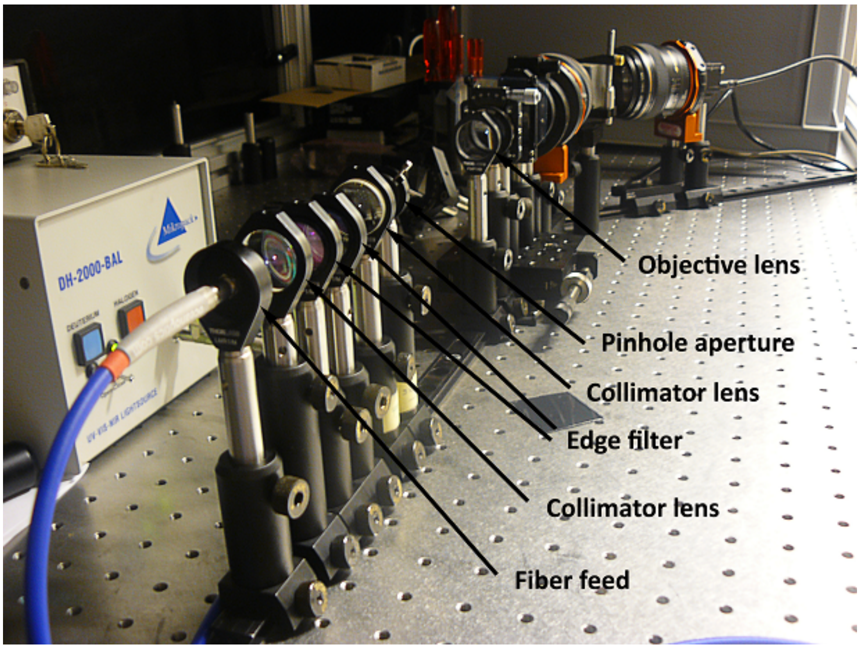

Figure 5.3: Photograph of the illumination system which focusses the light from the halogen source onto LOUPE's entrance aperture, after cutting the waveband by using a pair of edge filters.

responds to 8% of the length of the entire spectrum (which is 750 nm − 450 nm = 300 nm wide), or roughly 24 nm. Therefore, in order to meet the required 3 nm px^{-1}, another factor of 8 in spectral resolution is required, especially when the O_2A band is to be resolved. The fundamental limiting factor is the re-imaging quality of the Canon lens pair. A smaller spot size would decrease the minimal lateral distance between microspectra (thus allow for more dispersion), yet at the same time increase the resolution of the microspectra.

In the implementation of the second prism, spectra are stacked more closely together, which causes some lateral cross talk between spectra near 750 nm (see figure 5.4), so the microspectra can't be used in their totality. The usable part of the spectra measures roughly 6 px (32 μm) in width. This amounts to 2% of the total length, which roughly amounts to 3 nm. By using this prism, the combined effect of increased dispersion and the limited the bandwidth to regions where aberrations are small, the required spectral resolution can be reached.

5.3 Spectropolarimetric performance

Uniform and fully polarized input

To assess the spectropolarimetric performance of the instrument, two test environments were used. The first is the illumination system described above, with the addition of a wire-grid polarizer between the collimator lenses to produce a fully linearly polarized input. The results for this input using both prisms, is shown in figure 5.5.

In the current design, the instrument does not feature dual-channel capability. In order to characterize the full polarization spectrum, the polarization analyzer (see section 3.1) needs to be rotated by 90°. For each target setup, both channels thus had to be measured independently. Misalignments caused by rotation of the linear polarizer cause noticeable discrepancies between the intensities in different channels of the microspectra. However,

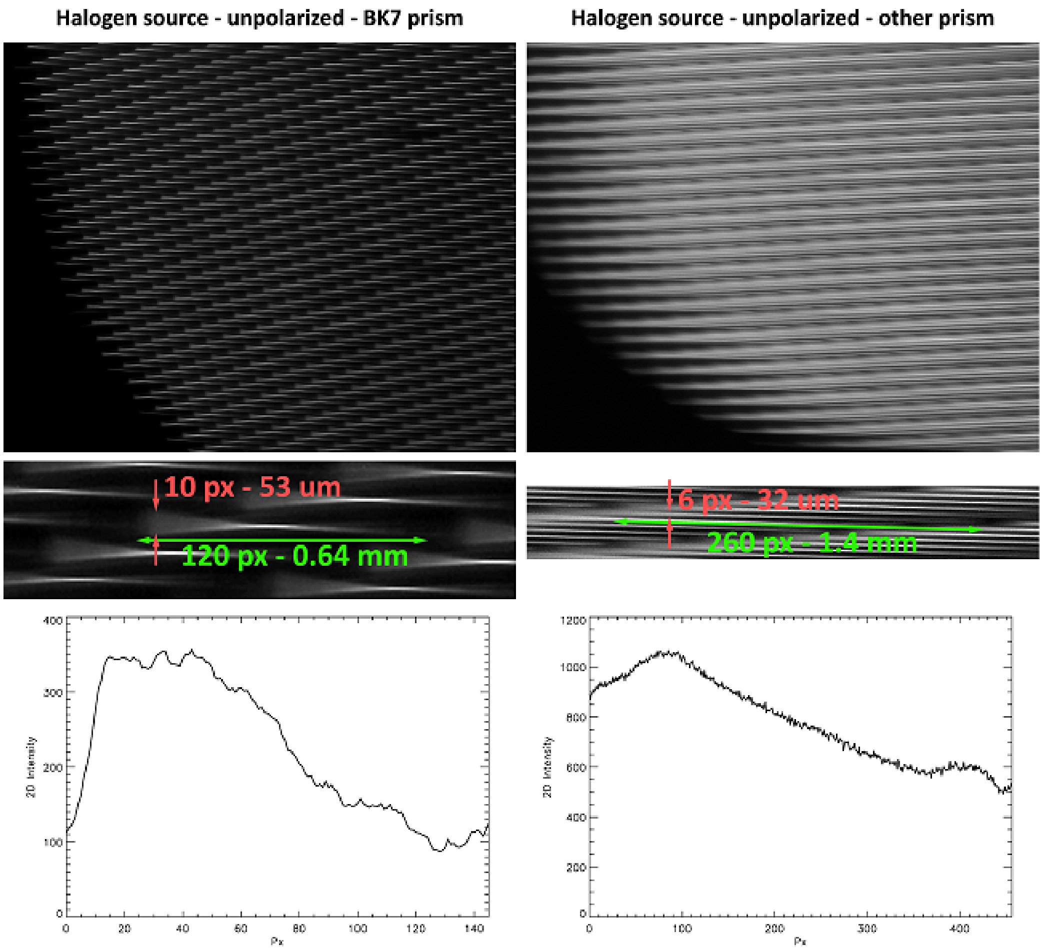

Figure 5.4: These plots show a pair of dark-corrected measurements acquired with the prototype setup of LOUPE-2A, of an unpolarized, uniformly illuminated field. The middle panels show magnifications of the same region on the chip, with the approximate dimension of the spectrum overlayed. The bottom plots show the spectral profiles of each of these microspectra, after they were cut out of the frame, and co-added in the vertical direction to produce 1-dimensional intensity spectra. The wavelength range of the implementation with the BK7-prism was restricted to 450 – 750 nm. The stacking efficiency and spectral resolution are limited by the fanning out of the microspectra towards 750 nm, where the spectrum measures 10 px in width. The wavelength range of the implementation featuring the other prism was limited to 600 – 750 nm. In this case, the microspectra were more closely stacked so that the extra dispersion generated by this prism could be afforded. The exposure times of the left and right images were 34 ms and 250 ms respectively, which reflects the fact that the higher dispersion spreads the flux over more pixels.

such differences are largely mitigated when considering the visibilities of the polarization modulations, which are shown in the lower panels of figures 5.5 and similar in figures elsewhere.

From figure 5.5 it becomes clear that the efficiency of the measurement is not optimal and that it is wavelength-dependent. 100% polarized input is expected to induce a modulation visibility with unit amplitude across all wavelengths. The setup featuring the BK7 prism shows near-perfect contrast in the blue part of the band, but a clear decrease of efficiency towards red wavelengths. The overall efficiency of the setup featuring the other prism is slightly lower. It seems to be constant with wavelength, but this can likely be attributed to the fact that the wavelength regime is much smaller in this case, so that broadband

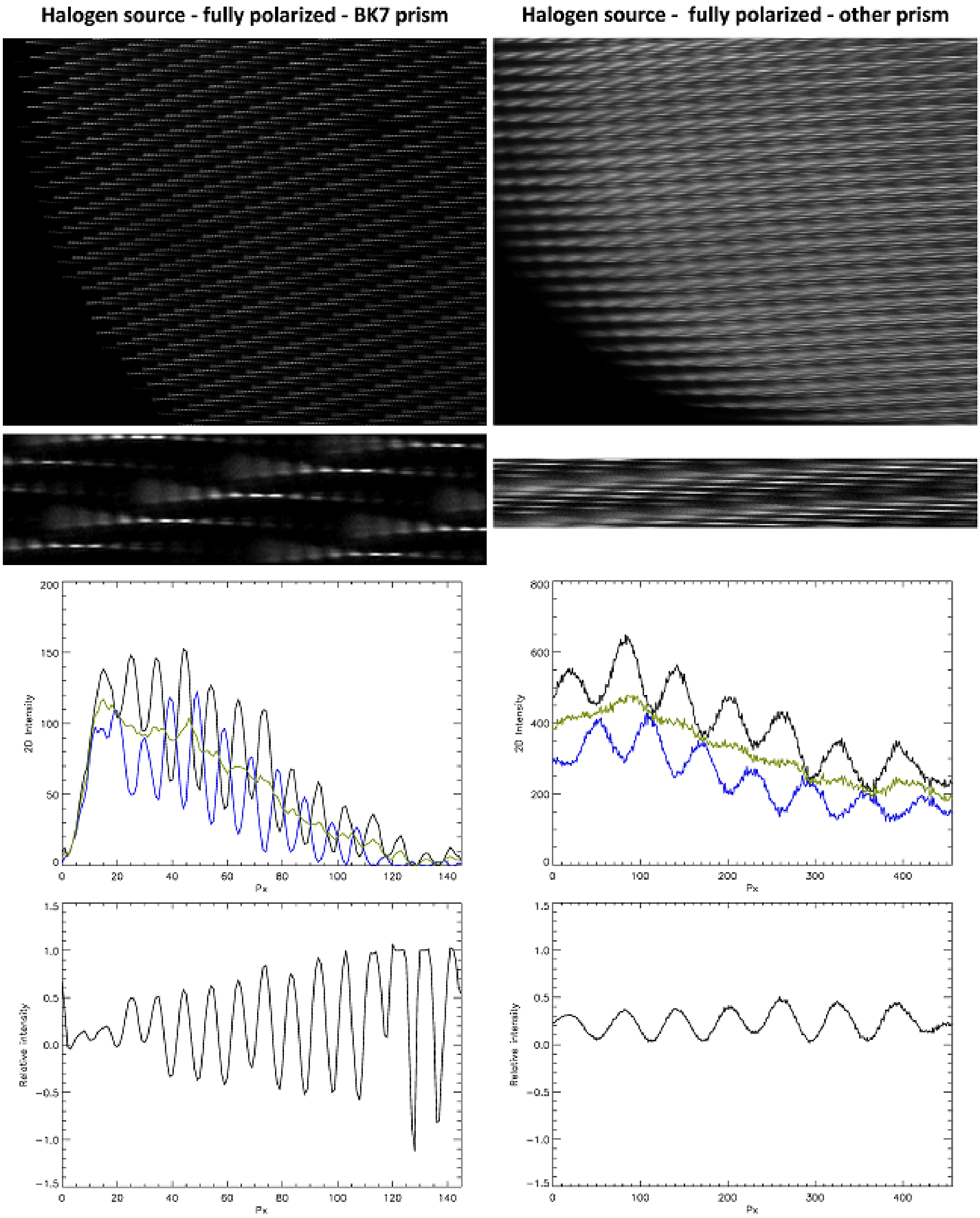
Halogen source - fully polarized - BK7 prism

Halogen source - fully polarized - other prism

Figure 5.5: These plots are analogous to the plots shown in figure 5.4, but now a wire-grid polarizer was placed in the illumination system to fully polarize the input. The microspectra which were cut out and magnified are the same as before (same location and same exposure time). In both cases, the polarization modulation profiles are clearly visible. The plots show both polarization channels in black and blue, and their average which constitute the original spectrum s_0. The lower plots show the visibilities of the modulation patterns. The measurements suffer from mismatches between the two polarization channels, and from a loss of efficiency towards shorter wavelengths.

wavelength-dependent features are less pronounced.

Loss of efficiency towards the red edge of the wavelength regime is likely a combination of effects associated with the various optics in the instrument, of which the performance breaks down towards longer wavelengths. The extinction ratio of both wire-grid polarizers used in this setup (one to polarize the input beam and one in the application of SPEX)

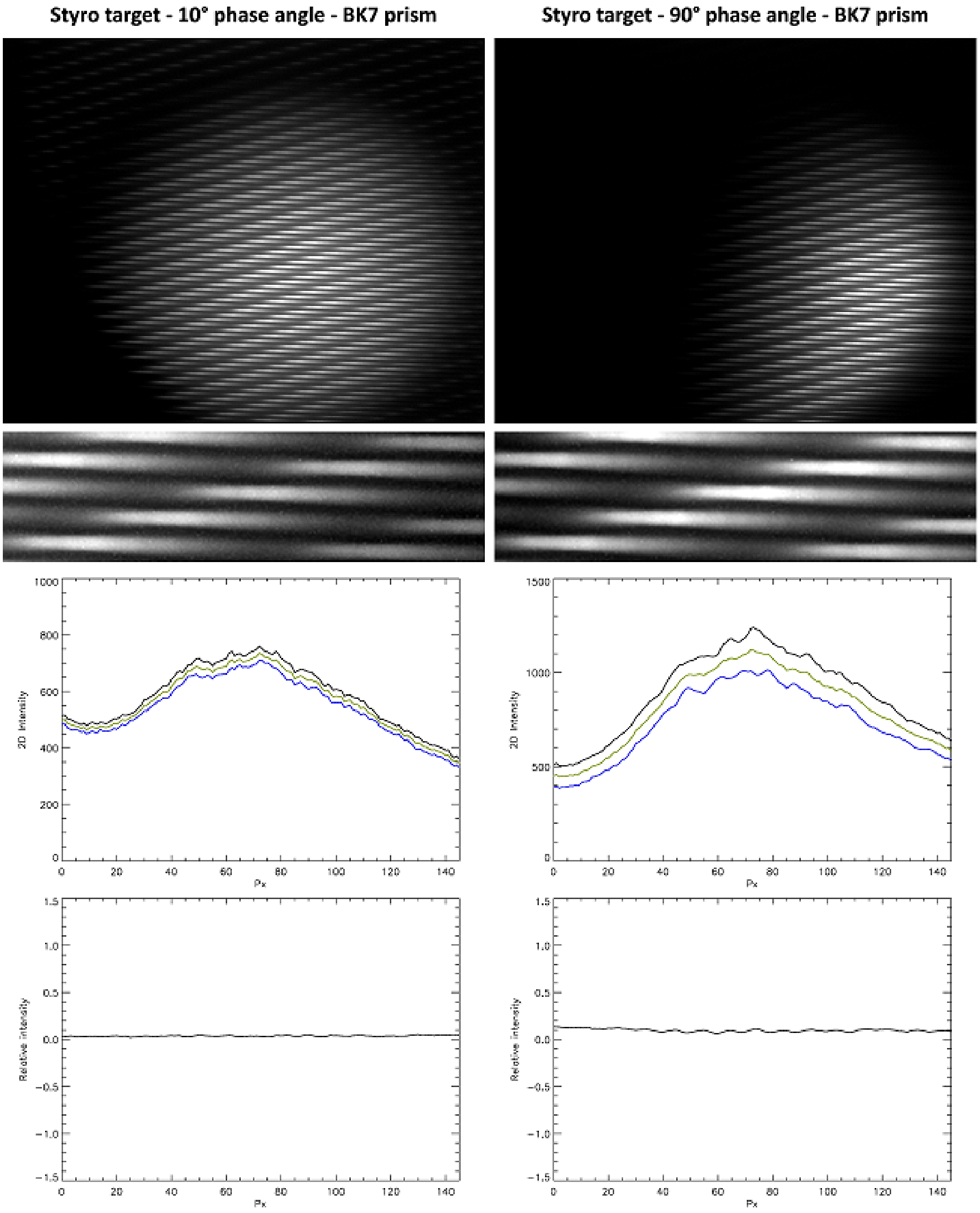

Figure 5.6: These plots are again analogous to the other two pair but this time, the instrument was not illuminated by the halogen source, but instead looked at the stryrophome target at phase angles of approximately 0° (left) and 90° (right), using only the BK7 prism. Again, the dark-corrected 1-D spectra and their visibility profiles are shown in the plots below. The integration times of both these measurements were 100ms. P_L being a lot lower than before, the visibility curves appear nearly flat. However, at 90° phase, the modulation is clearly visible. This pattern is enlarged and compared with four other samples across the disk in figure 5.8.

drops between $700 - 750$ nm (see figure 5.7). Towards 750 nm, the setup loses its ability to efficiently filter the circulary polarized component of the beam which exits the MOR (see figure 3.1). At the same time, the breakdown of the polarizer causes the degree of polarization of the source to decrease significantly, which approaches 0 beyond 750 nm. Finally, the zero-order QWP is only has a 0.25λ retardance close to 633 nm. At wavelengths significantly greater or lower than 633 nm, the QWP does not efficiently transform the linearly polarized input into circular polarization (again, see figure 3.1), so on these three accounts, the efficiency of the measurement is expected to decrease towards the edges of the band. However, as long as the polarization state of the input is known, the combination of these performance-variations can be characterized and calibrated for. After calibration, a low efficiency would cause higher noise in the polarization measurement, so longer integration times would be required. Since it is clear that photons are plenty (see section 3.2), efficiency variations are not expected to be a problem as long as they can be calibrated out.

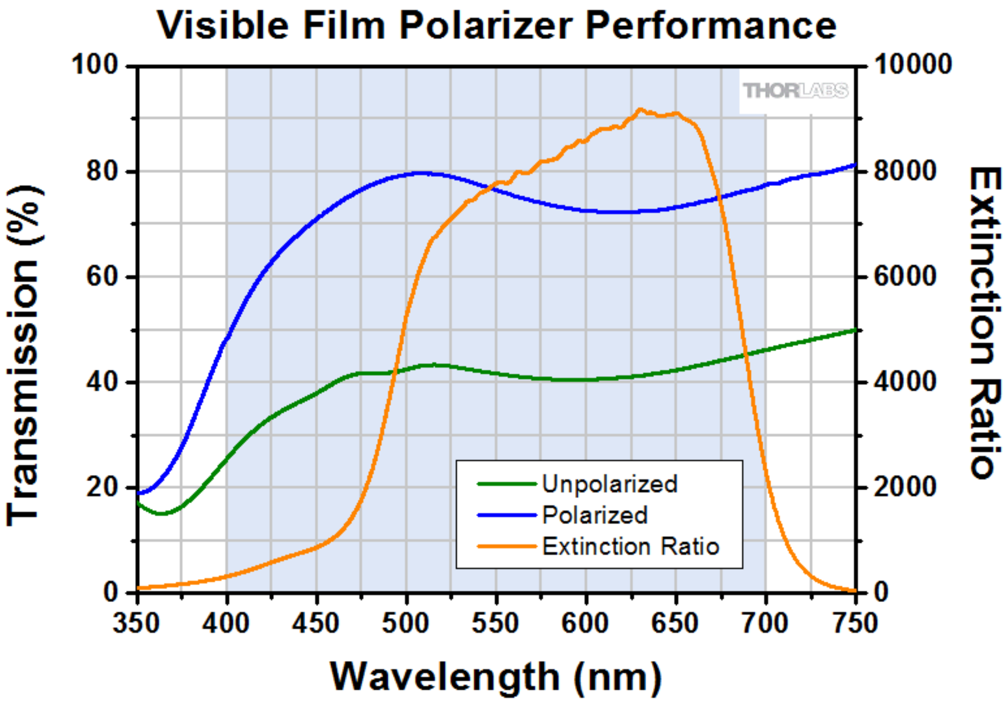

Figure 5.7: The performance of the wire-grid polarizers. The extinction ratio of the transmitted and absorbed beams quickly drops between $700 - 750$ nm and thus approaches 0 at the edge of the current wavelength regime, which spans between $450 - 750$ nm. This graph was adopted from the product description webpage provided by Thorlabs.

Loss of efficiency however, is not the only cause for a loss of contrast at the edge of the band. The re-imaging optics clearly aberrates the microspectra at longer wavelengths, which causes a loss in spectral resolution. The largest spot size for the BK7-prism is approximately 10 px (figure 5.5), which is comparable to the period of the modulation pattern. Hence, towards 750 nm, the polarization modulation can no longer be resolved. Unlike the efficiency of the polarization optics, undersampling of the modulation pattern due to aberrations of the re-imaging optics constitutes a loss of information which can not be calibrated for. The implementation of better optics is needed to mitigate these aberrations. Evidently, the same effect occurs towards blue wavelengths, but here, aberrations are not as severe.

5.3.1 Styrophome target

The second target is the stryrophome sphere which was also used to characterize the response of the implementation of LOUPE-1A (see section 3.2) for which the result is shown in figure 3.10. For this setup, only the BK7 prism was used because the smaller bandwidth combined with a higher dispersion associated with the other prism prohibitively limited the amount of light received per pixel. The result is shown in figure 5.6.

Figure 5.6 shows results for this target at two phase angles of approximately 0° and 90°. The spectra for which the analysis is shown in the lower panels, are of the same location in the field. Evidently, the polarization modulation is much less pronounced compared to the observations shown in figure 5.5 because, in this scattering configuration, P_L is expected to be of the order of 10%. The amplitude of the modulation is lower for 0° phase angle which, considering the models shown in figure 1.5 is also in line with the expectations.

P_L is expected to show variations across the surface of the styrophome sphere which with the current spatial resolution, can easily be visualized. Our interest in spatial variations of the polarization state is, after all the primary reason for most of our effort in the development of LOUPE. Figure 5.8 shows the visibility profiles for 4 microspectra, taken from different places across the disk. This plot plot shows that although the target is uniform (the styrophome sphere has no surface features analogous to landmasses and oceans), P_L decreases towards the limb of the disk.

We conclude this analysis by noting that due to an absence of a robust calibration and data reduction pipeline, we are unable to further quantify the polarization properties of the results presented here. The plots in figures 5.5, 5.6 and 5.8 unambiguously show the presence of polarized components, but in order to perform actual measurements of the quantities $P_L(\lambda)$ and $\phi_L(\lambda)$ and determine the quality of these measurements, the fitting scheme introduced in section 3.1 should first be implemented and tested.

5.4 Comparison with science goals

Despite the qualitative nature of the analysis above, meaningful conclusions regarding the relationship between the current prototype and the overarching science drivers can be drawn. The table below again summarizes the 11 science goals which were defined in chapter 2, and briefly discusses the extent to which the current prototype is able to satisfy them, wherever applicable.

ID	**Keywords**	**Current state**	**Comment**
R1	Disk-integration	Achieved	From the surface of the moon, the Earth spans 2° on the sky. The FOV of 20° by 20° will always contain the full disk, provided that the instrument can be pointed towards Earth adequately after landing on the Moon.
R2	Lifetime	N/A	
R3	Exposure time	Achieved	Integration times for observations on laboratory targets are in the order of 1 second which means that in the allocated time there is adequate opportunity for multiple integrations and calibration measurements between observations if needed.
R4	Wavelength coverage	Feasible	The amount of spectral dispersion is limited by the lateral size of the microspectra, which is determined by the imaging quality of the re-imaging system. The current setup features a pair of commercial photocamera objectives, which will need to be replaced with custom designed lenses or mirrors which are better optimized for blue and red wavelengths. Also, the optics should be chosen such that it has sufficient efficiency at the edges of the band. The current wavelength range is nearly $450 - 750$ nm, 50 nm short on both ends of the band.
R5	Coverage of the O_2A band	Feasible	The spectral resolution of the current setup near this wavelength is rougly 24 nm, which is the limit imposed by aberrations due to the re-imaging lenses. Improvement of the optics will lead to better spatial resolution and will allow the O_2A band to be included in the wavelength regime. See **R4**.
R6	Spectro-polarimetric resolution	Feasible	In order to properly sample the modulation profiles, the spectropolarimetric resolution should be improved to 3 nm px^{-1} while maintaining full dispersion.
R7	Spectro-polarimetric accuracy	Unknown	Efforts must be made to extract the polarization parameters $I(\lambda)$, $P_L(\lambda)$ and $\phi(\lambda)$ from the profiles shown in figures 5.5 and 5.6. After this, the response of the instrument to $P_L(\lambda)$ should be calibrated using sources with known polarization properties.
R8	Spectro polarimetric sensitivity	Feasible	The sensitivity of the instrument will likely be limited by photon shot-noise, which can be beat down to sufficiently low levels to allow for the sensitivity of 10^{-3} which is required, by increasing the integration time.
R9	Spatial resolution	Achieved	The MLA chosen for this setup slices the 20° by 20° FOV into 56 by 56 field points, each spanning 0.4° on the sky.
R10	Radiometric accuracy	Unknown	In this study, radiometric capabilities of the setup were not investigated and are deferred until the following iteration.
R11	Restriction on the size, weight, power and data transfer budget	Feasible	The current setup is ~ 42 cm in length. Both weight and size are dominated by the Canon objective lenses which were not designed with space applications in mind. The use of specially designed optics can be expected to decrease the size and weight of the instrument significantly. All optics are exptected to be solid state, so only the CMOS detector consumes power. CMOS technology allows selective read-out of the field, so that only the small fraction of the field which actually contains the Earth's disk need to be transmitted to Earth.

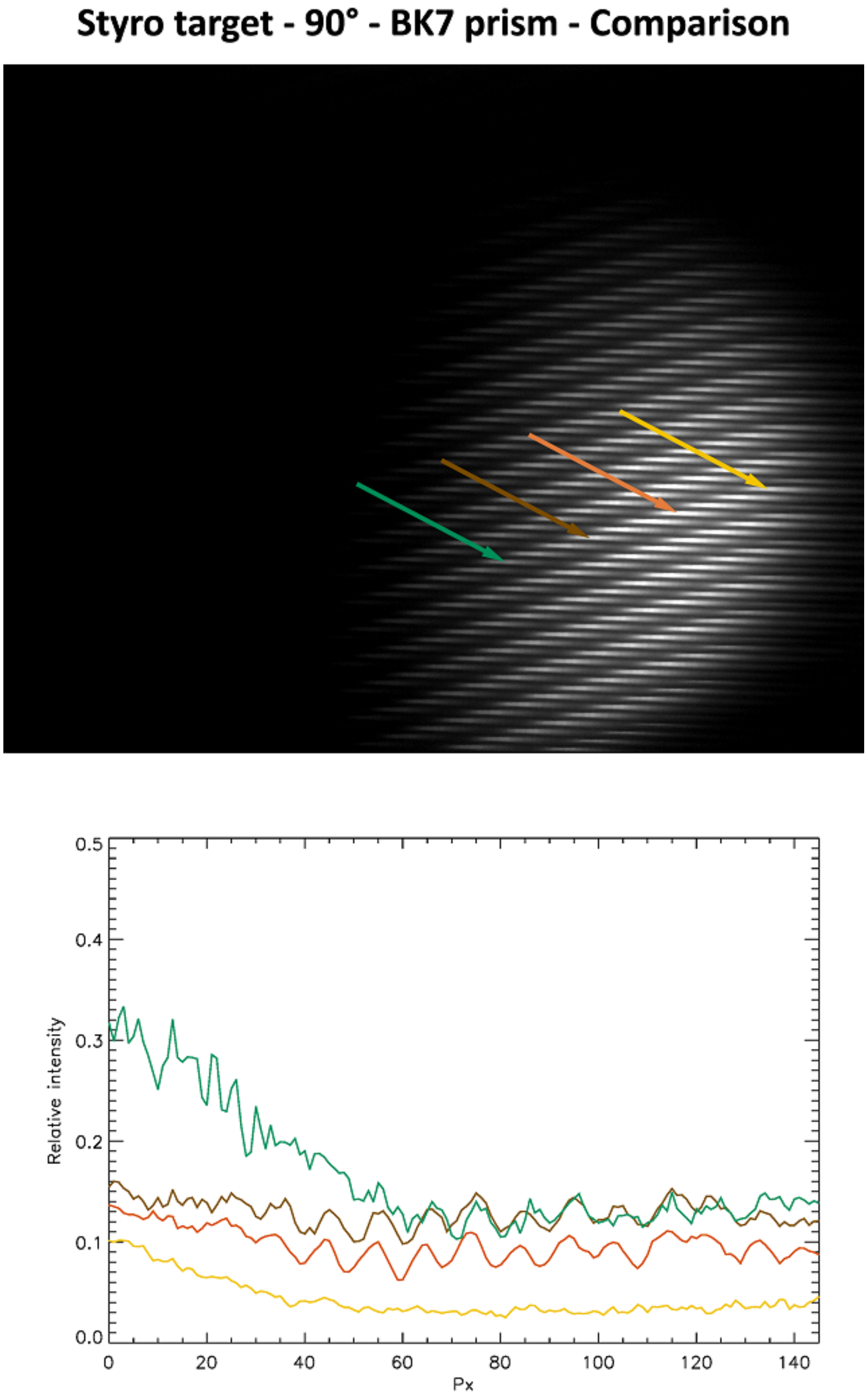

Figure 5.8: Comparison of the visibility profiles of the polarization modulation at different locations on the disk of the target. The coloured arrows correspond to the locations from which the coloured profiles were sampled. P_L increases towards the center of the visible part of the disk (red line) and the noise is seen to increase for spectra which are fainter.

Chapter 6

Conclusion

6.1 Summary

This thesis describes the design and development of a prototype for LOUPE, based on an evaluation of the scientific requirements put forth by Karalidi et al. (2012). LOUPE is to perform disk-integrated measurements of the degree and angle of linear polarization (P_L and ϕ_L) across visible wavelengths. These parameters contain vast amounts of information about the scattering properties of the surface and atmospheric constituents of planets and are not only crucial for our understanding of future exoplanet data, but also the Earth's climate system. Current radiative transfer models of exoplanets greatly lack independent validation, and the debate on global climate change critically suffers from lack of information regarding the global average values of parameters like albedo and atmospheric aerosol load. From the surface of the Moon, LOUPE will be in the perfect position to provide a significant contribution to both fields using a small, robust imaging spectropolarimeter.

Based on the work done by Karalidi et al. (2012), the science case was translated to a set of top-level requirements on the instrument, described in chapter 2. Building from the SPEX setup, we constructed a prototype for LOUPE which has the ability to observe the Earth with 100% visibility without active pointing, and which features a spatial resolution which is such that the contribution of continent-sized surface structures to the global polarization signature can be separately identified and analyzed. Using a pair of prisms, two implementations of the spectroscopic component were explored, one allowing for high resolution spectropolarimetry between $600 - 750$ nm, and one allowing for lower resolution spectropolarimetry between $450 - 750$ nm. Both implementations are capable of accepting a wide field of view of $20°$ by $20°$, but were adapted to accommodate a smaller field in which the Moon as seen from the Earth is imaged with the same scale as the Earth would be imaged as seen from the Moon. This adaptation involves only the replacement of the 35.2 mm objective lens of the system, with a lens which is 4 times as slow, without the need of altering the rest of the instrument. This modification is done in anticipation of test observations in which the target is the Moon itself.

6.2 Results

Although a quantitative investigation of the spectropolarimetric performance of the prototype has yet to be performed, the test observations performed thus far clearly confirm that the implementation of LOUPE as an imaging spectropolarimeter is highly feasible. The spectroscopic modulations due to the presence of a polarized component in light scattered off a spherical styrophome target are visibly discernible in the observations shown in figures 5.6 and 5.8. We were able to perform these observations across wavelength ranges which are close to what is ultimately desired, while fully satisfying the requirements imposed on the spatial resolution and the extent of the field, with integration times in the order of seconds. However during the development, some important issues came to light which need to be addressed in future iterations of the instrument.

The first of these is the notion that the spectral performance of the instrument, as well as the size and the weight, are directly limited by the re-imaging optic which at present, is implemented as a pair of commercially available photographic objective lenses. The flight model of LOUPE will feature dedicated optics which will be customly designed for the required specifications. One possible implementation is the replacement of these wide-field lens systems by off-axis parabolic mirrors, of which a schematic is shown in figure 6.1. Improving the spectral imaging performance while decreasing the size of the instrument is crucial in the further development of LOUPE.

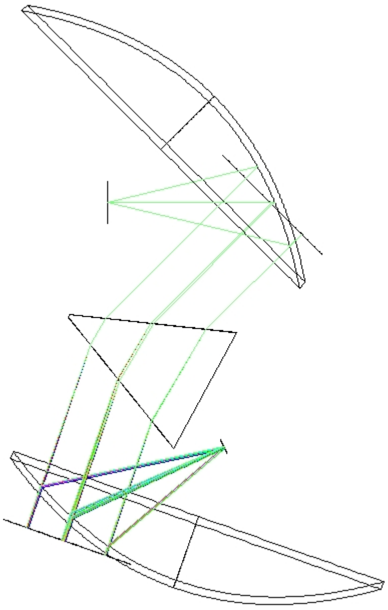

Figure 6.1: Raytracing simulation of a dispersive re-imaging system featuring off-axis parabolic mirrors instead of lenses. Mirrors have the advantage that they are a-chromatic and that they can facilitate a decrease of the instrument size by making more efficient use of the available space. Courtesy of Frans Snik.

The current setup relies on the manual rotation of a linear polarizer to sample both polarization channels. This defeats the notion that LOUPE is a solid state state instrument. It induces systematics associated with the physical alteration of the setup in time and it requires mechanical movement, which is undesirable in space. An obvious solution to this problem is the implementation of a polarization grating, which separates the two polarization channels and at the same time spectrally disperses the images. Not only would a polarization grating allow for a simultaneous and identical treatment of both polarization channels, but also provide the potential of significantly decreasing the size of the re-imaging system. Simultaneous imaging of both channels does require the need of a detector which is effectively twice as large. New optics would likely be needed to image the two beams in a way that they make optimal use of the available detector pixels.

To reach an absolute polarimetric accuracy of $\sim 1\%$, the instrument must be calibrated to that level. If calibration can be performed in-situ, calibration measurements can be acquired on a regular basis, in-between data acquisitions. However, it is not unthinkable that the instrument can only be calibrated once before the start of the mission, in which case it must be able to maintain stability at the 1% level through all phases of the mission, including launch and deployment on the Moon, which is challenging. On the other hand, an in-situ calibrator would add complexity to the instrument which might be undesirable. Regardless of the implementation, the stability requirement is likely to be one of the most important aspects of further study.

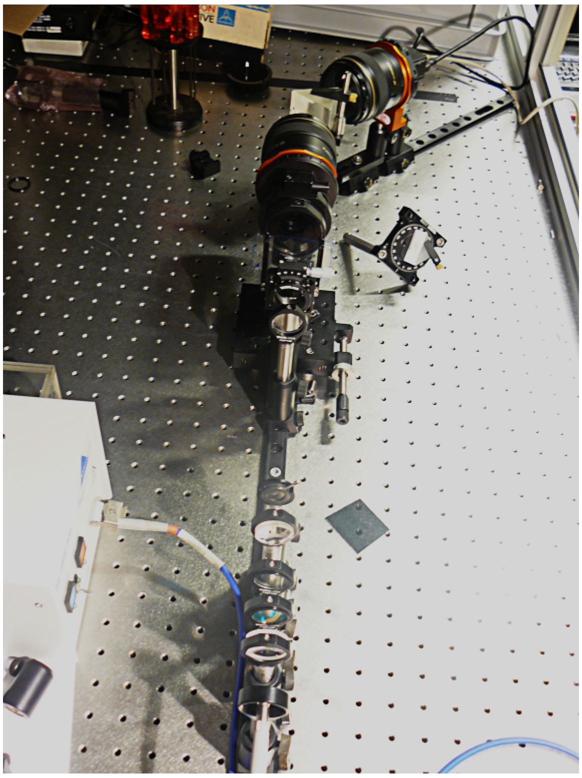

Figure 6.2: Photograph of the instrument in the latest stage of development, with the larger prism mounted between the re-imaging lenses. The smaller prism is located off the side of the instrument.

6.3 Future work

The front-optics of the instrument was implemented such that the instrument is suitable for measuring the polarization spectrum of the Moon. Before these observations can be performed, some issues must first be addressed:

1. In the current implementation, independent measurements of the two polarization channels causes severe systematics. A system must be implemented in which alignment errors are less severe, or in which quick alignment diagnostics can be performed.

2. The performance analysis presented in chapter 5, relied on a qualitative appraisal of the measurement results. A pipeline which collects, reduces and analyzes the data automatically must first be developed. An important aspect of this is automatic segmentation of the image to separate each of the microspectra, as well as the process of binning the data and fitting the sinusoidal modulation of equation 3.1.

3. Both the wavelength and absolute polarimetry must be extensively calibrated in the lab using line-lamps and sources with well known polarization characteristics.

4. The instrument must be re-assembled and mounted on a robust alt-azimuth mount.

After these lunar measurements, much more work is evidently needed to further develop this instrument. Most notably, issues regarding the improvement of the optics, calibration (pre-flight versus in-situ), implementation of radiometric capabilities, miniaturization and space qualification of the instrument must be addressed. Nonetheless, this prototype has already satisfied a number of elementary requirements. Taking into account the fact that most of the optics used in this iteration is commercially available off the shelf, combined with the notion that the size of the instrument (42 cm) can be considered modest, gives good hopes for a prosperous continuation of the LOUPE project.

Bibliography

Climate Change 2001: The Scientific Basis. Contribution of Working Group I to the Thirs Assessment Report of the Intergovernmental Panel on Climate Change, (eds. J. T. Houghton, Y. Ding, D. J. Griggs, M. Noguer, P. J. van der Linden et al.). 2001.

J. Antichi, K. Dohlen, R. G. Gratton, D. Mesa, R. U. Claudi, E. Giro, A. Boccaletti, D. Mouillet, P. Puget, and J.-L. Beuzit. BIGRE: A Low Cross-Talk Integral Field Unit Tailored for Extrasolar Planets Imaging Spectroscopy. ApJ, 695:1042–1057, April 2009. doi: 10.1088/0004-637X/695/2/1042.

A. Bazzon, H. M. Schmid, and D. Gisler. Measurement of the earthshine polarization in the B, V, R, and I band as function of phase. *ArXiv e-prints*, June 2013.

Frida A-M. Bender, Henning Rodhe, Robert J. Charlson, Annica M. L. Ekman, and Norman Loeb. 22 views of the global albedocomparison between 20 gcms and two satellites. *Tellus A*, 58(3):320–330, 2006. ISSN 1600-0870. doi: 10.1111/j.1600-0870.2006.00181.x. URL `http://dx.doi.org/10.1111/j.1600-0870.2006.00181.x`.

L. Brown. Experimental line parameters of the oxygen A-band at 760 nanm. *J Mol Spectrosc*, 199, February 2000.

James D. Carroll. A new definition of life. *Chirality*, 21(3):354–358, 2009. ISSN 1520-636X. doi: 10.1002/chir.20590. URL `http://dx.doi.org/10.1002/chir.20590`.

E. Duursma and M. Boisson. Global oceanic and atmospheric oxygen stability considered in relation to the carbon cycle and to different time scales . *Oceanologica Acta*, 17:117–141, March 1994.

P. Falkowski, R. J. Scholes, E. Boyle, J. Canadell, D. Canfield, J. Elser, N. Gruber, K. Hibbard, P. Hgberg, S. Linder, F. T. Mackenzie, B. Moore III, T. Pedersen, Y. Rosenthal, S. Seitzinger, V. Smetacek, and W. Steffen. The global carbon cycle: A test of our knowledge of earth as a system. *Science*, 290(5490):291–296, 2000. doi: 10.1126/science.290.5490.291. URL `http://www.sciencemag.org/content/290/5490/291.abstract`.

L. Fossati, C. A. Haswell, C. S. Froning, L. Hebb, S. Holmes, U. Kolb, C. Helling, A. Carter, P. Wheatley, A. Collier Cameron, B. Loeillet, D. Pollacco, R. Street, H. C. Stempels, E. Simpson, S. Udry, Y. C. Joshi, R. G. West, I. Skillen, and D. Wilson. Metals in the Exosphere of the Highly Irradiated Planet WASP-12b. ApJ, 714:L222–L227, May 2010. doi: 10.1088/2041-8205/714/2/L222.

J. D. Fraine, D. Deming, M. Gillon, E. Jehin, B.-O. Demory, B. Benneke, S. Seager, N. K. Lewis, H. Knutson, and J.-M. Désert. Spitzer Transits of the Super-Earth GJ1214b and Implications for its Atmosphere. ApJ, 765:127, March 2013. doi: 10.1088/0004-637X/765/2/127.

Y. Fujii and H. Kawahara. Mapping Earth Analogs from Photometric Variability: Spin-Orbit Tomography for Planets in Inclined Orbits. ApJ, 755:101, August 2012. doi: 10.1088/0004-637X/755/2/101.

B. Hapke, R. Nelson, and W. Smythe. The Opposition Effect of the Moon: Coherent Backscatter and Shadow Hiding. Icarus, 133:89–97, May 1998. doi: 10.1006/icar.1998.5907.

B. W. Hapke, R. M. Nelson, and W. D. Smythe. The opposition effect of the moon - The contribution of coherent backscatter. *Science*, 260:509–511, April 1993. doi: 10.1126/science.260.5107.509.

Stephen Jones, Frank Iannarilli, and Paul Kebabian. Realization of quantitative-grade fieldable snapshot imaging spectropolarimeter. *Opt. Express*, 12(26):6559–6573, Dec 2004. doi: 10.1364/OPEX.12.006559. URL `http://www.opticsexpress.org/abstract.cfm?URI=oe-12-26-6559`.

T. Karalidi and D. M. Stam. Modeled flux and polarization signals of horizontally inhomogeneous exoplanets applied to Earth-like planets. A&A, 546:A56, October 2012. doi: 10.1051/0004-6361/201219297.

T. Karalidi, D. M. Stam, F. Snik, S. Bagnulo, W. B. Sparks, and C. U. Keller. Observing the Earth as an exoplanet with LOUPE, the Lunar Observatory for Unresolved Polarimetry of Earth. *ArXiv e-prints*, March 2012.

D. Kim and V. Ramanathan. Improved estimates and understanding of global albedo and atmospheric solar absorption. Geophys. Res. Lett., 39:L24704, December 2012. doi: 10.1029/2012GL053757.

G. Kopp and J. L. Lean. A new, lower value of total solar irradiance: Evidence and climate significance. Geophys. Res. Lett., 38:L01706, January 2011. doi: 10.1029/2010GL045777.

N. Madhusudhan, J. Harrington, K. B. Stevenson, S. Nymeyer, C. J. Campo, P. J. Wheatley, D. Deming, J. Blecic, R. A. Hardy, N. B. Lust, D. R. Anderson, A. Collier-Cameron, C. B. T. Britt, W. C. Bowman, L. Hebb, C. Hellier, P. F. L. Maxted, D. Pollacco, and R. G. West. A high C/O ratio and weak thermal inversion in the atmosphere of exoplanet WASP-12b. Nature, 469:64–67, January 2011. doi: 10.1038/nature09602.

C. Majeau, E. Agol, and N. B. Cowan. A Two-dimensional Infrared Map of the Extrasolar Planet HD 189733b. ApJ, 747:L20, March 2012. doi: 10.1088/2041-8205/747/2/L20.

C. H. Mayer, T. P. McCullough, and R. M. Sloanaker. Observations of Venus at 3.15-CM Wave Length. ApJ, 127:1, January 1958. doi: 10.1086/146433.

M. Mayor, D. Queloz, G. Marcy, P. Butler, R. Noyes, S. Korzennik, M. Krockenberger, P. Nisenson, T. Brown, T. Kennelly, C. Rowland, S. Horner, G. Burki, M. Burnet, and M. Kunzli. 51 Pegasi. IAU Circ., 6251:1, October 1995.

M. I. Mishchenko and Glory APS Science Team. Polarimetric remote sensing of the Earth from satellites: a perspective. *AGU Fall Meeting Abstracts*, page F1632, December 2011.

M. I. Mishchenko, B. Cairns, G. Kopp, C. F. Schueler, B. A. Fafaul, J. E. Hansen, R. J. Hooker, T. Itchkawich, H. B. Maring, and L. D. Travis. Accurate Monitoring of Terrestrial Aerosols and Total Solar Irradiance: Introducing the Glory Mission. *Bulletin of the American Meteorological Society*, 88:677, 2007. doi: 10.1175/BAMS-88-5-677.

D. B. Mott, S. Aslam, K. A. Blumenstock, R. K. Fettig, D. E. Franz, A. S. Kutyrev, M. J. Li, C. J. Monroy, S. H. Moseley, and D. S. Schwinger. Magnetically actuated microshutter arrays. In M. E. Motamedi and R. Goering, editors, *Society of Photo-Optical Instrumentation Engineers (SPIE) Conference Series*, volume 4561 of *Society of Photo-Optical Instrumentation Engineers (SPIE) Conference Series*, pages 163–170, October 2001.

Kazuhiko Oka and Takayuki Kato. Spectroscopic polarimetry with a channeled spectrum. *Opt. Lett.*, 24(21):1475–1477, Nov 1999. doi: 10.1364/OL.24.001475. URL `http://ol.osa.org/abstract.cfm?URI=ol-24-21-1475`.

Ya. V. Pavlenko, J. S. Jenkins, H. R. A. Jones, O. Ivanyuk, and D. J. Pinfield. Effective temperatures, rotational velocities, microturbulent velocities and abundances in the atmospheres of the sun, hd 1835 and hd 10700. *Monthly Notices of the Royal Astronomical Society*, 422(1):542–552, 2012. doi: 10.1111/j.1365-2966.2012.20629.x. URL `http://mnras.oxfordjournals.org/content/422/1/542.abstract`.

I. A. G. Snellen, R. J. de Kok, E. J. W. de Mooij, and S. Albrecht. The orbital motion, absolute mass and high-altitude winds of exoplanet HD209458b. Nature, 465:1049–1051, June 2010. doi: 10.1038/nature09111.

F. Snik, T. Karalidi, and C. U. Keller. Spectral modulation for full linear polarimetry. *ArXiv e-prints*, March 2009.

W. Sparks, T. A. Germer, J. W. MacKenty, and F. Snik. Compact and robust method for full Stokes spectropolarimetry. Appl. Opt., 51:5495, August 2012. doi: 10.1364/AO.51.005495.

W.B. Sparks, J.H. Hough, L. Kolokolova, T.A. Germer, F. Chen, S. DasSarma, P. DasSarma, F.T. Robb, N. Manset, I.N. Reid, F.D. Macchetto, and W. Martin. Circular polarization in scattered light as a possible biomarker. *Journal of Quantitative Spectroscopy and Radiative Transfer*, 110(1416):1771 – 1779, 2009. ISSN 0022-4073. doi: 10.1016/j.jqsrt.2009.02.028. URL `http://www.sciencedirect.com/science/article/pii/S0022407309000909`. ¡ce:title¿XI Conference on Electromagnetic and Light Scattering by Non-Spherical Particles: 2008¡/ce:title¿.

D. M. Stam. Spectropolarimetric signatures of Earth-like extrasolar planets. A&A, 482: 989–1007, May 2008. doi: 10.1051/0004-6361:20078358.

M. F. Sterzik, S. Bagnulo, and E. Palle. Biosignatures as revealed by spectropolarimetry of Earthshine. Nature, 483:64–66, March 2012. doi: 10.1038/nature10778.

O. Struve. Proposal for a project of high-precision stellar radial velocity work. *The Observatory*, 72:199–200, October 1952.

M. R. Swain, G. Tinetti, G. Vasisht, P. Deroo, C. Griffith, J. Bouwman, P. Chen, Y. Yung, A. Burrows, L. R. Brown, J. Matthews, J. F. Rowe, R. Kuschnig, and D. Angerhausen. Water, Methane, and Carbon Dioxide Present in the Dayside Spectrum of the Exoplanet HD 209458b. ApJ, 704:1616–1621, October 2009. doi: 10.1088/0004-637X/704/2/1616.

Y. I. Velikodsky, N. V. Opanasenko, L. A. Akimov, V. V. Korokhin, Y. G. Shkuratov, V. G. Kaydash, G. Videen, S. A. Ehgamberdiev, and N. E. Berdalieva. New Earth-based absolute photometry of the Moon. Icarus, 214:30–45, July 2011. doi: 10.1016/j.icarus.2011.04.021.